IMMUNOTHERAPY

Design of a potent interleukin-21 mimic for cancer immunotherapy

Jung-Ho Chun[1,2,3]†, Birkley S. Lim[4,5]†, Suyasha Roy[6]†, Michael J. Walsh[4,5]†, Gita C. Abhiraman[7]†, Kevin Zhangxu[4,5], Tavus Atajanova[4,5], Or-Yam Revach[8,9], Elisa C. Clark[10], Peng Li[6], Claire A. Palin[8], Asheema Khanna[11], Samantha Tower[11], Rakeeb Kureshi[5,12], Megan T. Hoffman[5,12], Tatyana Sharova[13,14], Aleigha Lawless[13,14], Sonia Cohen[13,14], Genevieve M. Boland[9,13,14], Tina Nguyen[1], Frank Peprah[4,5], Julissa G. Tello[4,5], Samantha Y. Liu[5], Chan Johng Kim[1,2], Hojeong Shin[1,2], Alfredo Quijano-Rubio[1]‡, Kevin M. Jude[7], Stacey Gerben[1], Analisa Murray[1], Piper Heine[1], Michelle DeWitt[1], Umut Y. Ulge[1], Lauren Carter[1], Neil P. King[1,2], Daniel-Adriano Silva[1]‡, Hao Yuan Kueh[10], Vandana Kalia[11,15], Surojit Sarkar[11,15,16], Russell W. Jenkins[8,9], K. Christopher Garcia[7,17], Warren J. Leonard[6]*, Michael Dougan[4,18]*, Stephanie K. Dougan[5,12]*, David Baker[1,2,19]*

Long-standing goals of cancer immunotherapy are to activate cytotoxic antitumor T cells across a range of affinities for tumor antigens while suppressing regulatory T cells. Computational protein design has enabled the precise tailoring of proteins to meet specific needs. Here, we report a de novo designed IL-21 mimic, 21h10, with high stability and signaling potency in humans and mice. In murine and ex vivo human organotypic tumor models, 21h10 showed robust antitumor activity, with more prolonged signaling and stronger antitumor activity than native IL-21. 21h10 induced pancreatitis that could be mitigated by TNF blockade without compromising antitumor efficacy. Although antidrug antibodies to 21h10 formed, they were not neutralizing. 21h10 induced highly cytotoxic T cells with a range of affinities, robustly expanding intratumoral low-affinity cytotoxic T cells and driving high expression of IFN-γ and granzyme B compared with native IL-21, while increasing the frequency of IFN-γ$^+$ T helper 1 cells and reducing regulatory T cells. The full human-mouse cross-reactivity, high stability and potency, and low-affinity antitumor responses support the translational potential of 21h10.

INTRODUCTION

Interleukin-21 (IL-21) plays a key role in the differentiation of effector T cells (*1*–*4*), T follicular helper (T_{FH}) cells (*5*), B cells (*6*, *7*), natural killer (NK) cells (*3*), macrophages (*8*), and dendritic cells (*9*, *10*). IL-21 promotes the proliferation and survival of CD8 T cells and the generation of memory CD8 T cells (*10*–*13*). In addition, IL-21 enhances the effector functions of CD8 T cells (*10*, *14*) and cooperates with IL-15 to further promote the expansion of these cells (*4*). Multiple murine tumor models and early-stage clinical trials (*15*, *16*) of recombinant IL-21 have been completed in several types of cancer, including melanoma (*17*–*22*), renal cell carcinoma (*21*–*23*), ovarian cancer (*24*), and non-Hodgkin's lymphoma (*25*), both as a single agent and in combination with immune checkpoint inhibitors and cancer vaccines. These trials showed some evidence of efficacy, although less than contemporaneous trials of immune checkpoint inhibitors. IL-21 was also shown to be more effective than IL-2 when premelanosome protein (PMEL)–1 T cell receptor (TCR) transgenic CD8 T cells were cultured in vitro with cytokines before adoptive transfer into B16F10 melanoma-bearing mice (*26*). Although the initial clinical testing of IL-21–based cancer immunotherapies has been encouraging, the precise effect of IL-21 on antitumor responses remains incompletely understood. In addition, IL-21 has low stability, resulting in suboptimal pharmacokinetic properties, and the limited antitumor activity of human IL-21 (hIL-21) in mice has complicated the use of animal models to predict the toxicity and activity of candidate IL-21 therapeutics in humans (*27*–*31*).

Inspired by previous success in designing de novo IL-2 mimics for cancer immunotherapy (*32*, *33*), we reasoned that a de novo protein mimic of IL-21 with augmented stability that potently induces signaling in both humans and mice could overcome the limitations of native IL-21. We set out to use computational protein design to create IL-21 mimics with improved therapeutic properties. We developed 21h10, which is highly stable in vivo, shows efficacy against

[1]Institute for Protein Design, University of Washington, Seattle, WA, USA. [2]Department of Biochemistry, University of Washington School of Medicine, Seattle, WA, USA. [3]Graduate Program in Biological Physics, Structure and Design, University of Washington, Seattle, WA, USA. [4]Department of Medicine, Division of Gastroenterology, Massachusetts General Hospital, Boston, MA, USA. [5]Department of Cancer Immunology and Virology, Dana-Farber Cancer Institute, Boston, MA, USA. [6]Laboratory of Molecular Immunology and the Immunology Center, National Heart, Lung, and Blood Institute, National Institutes of Health, Bethesda, MD, USA. [7]Department of Molecular and Cellular Physiology, Stanford University School of Medicine, Stanford, CA, USA. [8]Mass General Cancer Center, Krantz Family Center for Cancer Research, Department of Medicine, Massachusetts General Hospital, Harvard Medical School, Boston, MA, USA. [9]Broad Institute of MIT and Harvard, Cambridge, MA, USA. [10]Department of Bioengineering and Institute for Stem Cell and Regenerative Medicine, University of Washington, Seattle, WA, USA. [11]Ben Towne Center for Childhood Cancer Research, Seattle Children's Research Institute, Seattle, WA, USA. [12]Department of Immunology, Harvard Medical School, Boston, MA, USA. [13]Massachusetts General Hospital Cancer Center, Harvard Medical School, Boston, MA, USA. [14]Department of Surgery, Massachusetts General Hospital, Boston, MA, USA. [15]Department of Pediatrics, University of Washington School of Medicine, Seattle, WA, USA. [16]Department of Pathology, University of Washington School of Medicine, Seattle, WA, USA. [17]Howard Hughes Medical Institute, Stanford University School of Medicine, Stanford, CA, USA. [18]Department of Medicine, Harvard Medical School, Boston, MA, USA. [19]Howard Hughes Medical Institute, University of Washington, Seattle, MA, USA.
†These authors contributed equally to this work.
‡Present address: Monod Bio, Seattle, WA, USA.
*Corresponding author. Email: leonardw@nhlbi.nih.gov (W.J.L.); michael_dougan@dfci.harvard.edu (M.D.); stephanie_dougan@dfci.harvard.edu (S.K.D.); dabaker@uw.edu (D.B.)

multiple murine models of cancer, and activates human T cells, including tumor-infiltrating lymphocytes, from patients with refractory melanoma.

RESULTS

Computational protein design of an IL-21 mimic

IL-21 signals by inducing heterodimerization of the IL-21 receptor (IL-21R) with the common cytokine receptor γ chain (γ_c), leading to the activation of Janus kinase 1 (JAK1) and JAK3, which are associated with the IL-21R and γ_c intracellular domains, respectively. This signaling results in the phosphorylation and activation of signal transducers and activators of transcription (STAT) transcription factors (*34*). Native IL-21 makes extensive interfaces with both receptor subunits (Fig. 1A) involving largely helical secondary structures, but the "backside" of IL-21 contains two long loops that we reasoned might reduce the stability of the molecule. Traditional protein engineering approaches that use directed evolution to identify small numbers of sequence changes are not able to replace extended structural segments such as these poorly ordered regions. Instead, we sought to construct mimics that retain the receptor-interacting interfaces, but with a more well-ordered and less protease-susceptible overall structure. Because the structure of the full complex was not initially available, we began from the hIL-21/human IL-21R (hIL-21/hIL-21R) complex structure (*35*) and docked the human γ_c ($h\gamma_c$) from the human IL-2 complex structure (*36*) on the hIL-21/hIL-21R complex structure. We then generated helical protein scaffolds with regions that superimpose perfectly on the receptor-interacting segments of native IL-21, but with improved interhelix packing, short connecting loops, and minimal unstructured regions.

Wild-type hIL-21 consists of four helices, with helix A (the first helix from the N terminus) and helix C (the third helix) interacting with hIL-21R and helix D (the fourth helix) interacting with $h\gamma_c$ (*36*, *37*). Helix B (the second helix) and helix C are not long enough to form ideal intramolecular interactions and intermolecular contacts with the receptor chains, so we replaced the two long unstructured regions between helix A/helix B and helix C/helix D by extending helix B and helix C. We sampled different helical bundle "up-down-up-down" topologies by testing different connectivities between the helices; these differ from the "up-up-down-down" topology of native IL-21 and allow more ideal helical packing and loop geometries. Sequences were designed for these backbones in the context of hIL-21R using *Rosetta*, retaining the residues interacting with hIL-21R and anticipated to interact with $h\gamma_c$. We stochastically generated designs with these properties using *Rosetta* helical sampling and loop-building methodology and selected for experimental characterization to validate their folding to the designed structure (fig. S1A).

An IL-21 mimic, 21h10, binds to human and murine IL-21Rs

We obtained synthetic genes for the selected designs and assessed binding to hIL-21R using yeast surface display. Four designs bound hIL-21R, but none bound to $h\gamma_c$ in the presence of hIL-21R (fig. S1B and table S1); this was not unexpected because of the unknown (at the time) $h\gamma_c$ structure, which was not incorporated in the design stage. From a mutagenesis library around the tightest binder, 21d26, we identified a variant, 21JC15, that binds $h\gamma_c$ weakly in an hIL-21R–dependent manner and murine γ_c ($m\gamma_c$) in a murine IL-21R (mIL-21R)–dependent manner (table S1). Further interface optimization guided by site-saturation mutagenesis and combinatorial library screening (fig. S1C) resulted in 21h10 with high affinity for both the human and murine IL-21R complexes (Fig. 1B and tables S1 and S2). 21h10 is shorter than hIL-21 (102 versus 131 amino acids) with sequence identity only in the conserved interface regions (*38*, *39*). 21h10 was expressed at high levels in *Escherichia coli* and monodisperse in size exclusion chromatography (Fig. 1C) and has a helical circular dichroism (CD) structure consistent with the design model. CD melting experiments revealed that 21h10 has high thermal stability, with a melting temperature (T_m) around 75°C (Fig. 1D).

Copurification of 21h10 with the hIL-21R extracellular domain, followed by mixing this complex with the extracellular domain of $h\gamma_c$ (amino acids 33 to 232), resulted in the growth of crystals that diffracted anisotropically with resolution between 2.3 and 3.4 Å (fig. S2 and table S3). The solution of the structure by molecular replacement revealed the structure of 21h10 in complex with hIL-21R and $h\gamma_c$ to be a Y-shaped receptor assembly similar to the wild-type hIL-21 complex (*37*). 21h10 binds to hIL-21R at site I through helices 2 and 3, burying a surface area of 870 $Å^2$, and it binds to $h\gamma_c$ at site IIa through helix 4, burying a surface area of 423 $Å^2$ (Fig. 1E and table S4). The key molecular contacts mediating receptor interaction are strongly conserved. At the site I interface, 21h10 interacts with hIL-21R through hydrogen bonds at residues K39, R46, R59, R63, and R65 and salt bridges at residues R42, R46, R53, and D69 (table S4). These side chains of 21h10 are nearly identically positioned to the corresponding side chains in hIL-21 despite different molecular topology (Fig. 1F). Similarly, at the site IIa interface, 21h10 binds to $h\gamma_c$ through sparse hydrogen bonding at residues S92 and Q95 on helix 4 (table S4). These two residues are precisely conserved in helix D of hIL-21 (Fig. 1F), reflecting the ability of de novo protein design to reproduce important molecular interactions in a protein-protein interface accurately.

21h10 potently induces STAT phosphorylation and effector CD8 T cell differentiation

Upon receptor binding, native IL-21 mediates downstream signaling by phosphorylating STAT1 and STAT3 in T cells (*40*). Whereas hIL-21 showed low cross-reactivity in murine cells (fig. S3A and table S5), 21h10 treatment in vitro led to phosphorylation of STAT1 and STAT3 with potency equivalent to native hIL-21 and mIL-21 in both human and murine CD8 T cells, CD4 T cells, and B cells (Fig. 2A, fig. S3B, and table S6).

Native IL-21 promotes effector CD8 T cell differentiation in human CD8 T cells ex vivo (*3*, *41*) and contributes to effector T cell ($CD44^+CD62L^-$) generation in vivo (*42*). To investigate the effects of 21h10 on gene expression and effector CD8 T cell differentiation, we cultured murine CD8 T cells in medium containing serum with 100 pM, 1 nM, 10 nM, and 100 nM mIL-21 or 21h10 and analyzed gene expression by RNA sequencing. 21h10 increased expression of effector molecules (*Tbx21*, *Prdm1*, *Prf1*, and *Gzmb*) while reducing the expression of the genes associated with a resting state (*Tcf7* and *Sell*) as compared with mIL-21 at 100 pM and 1 nM. 21h10 (100 pM) elicited a gene expression profile similar to that of 1 nM mIL-21 (Fig. 2B and fig. S3C); gene expression patterns were similar but not identical at higher doses (fig. S3D). 21h10 elicited similar or higher IL-21R and granzyme B protein expression levels in human and murine CD8 T cells compared with hIL-21 and mIL-21, respectively (fig. S4A), and proliferation of murine CD8 T cells at 1 nM and 100 pM 21h10 was enhanced compared with mIL-21 (fig. S4, B to C). 21h10 promoted

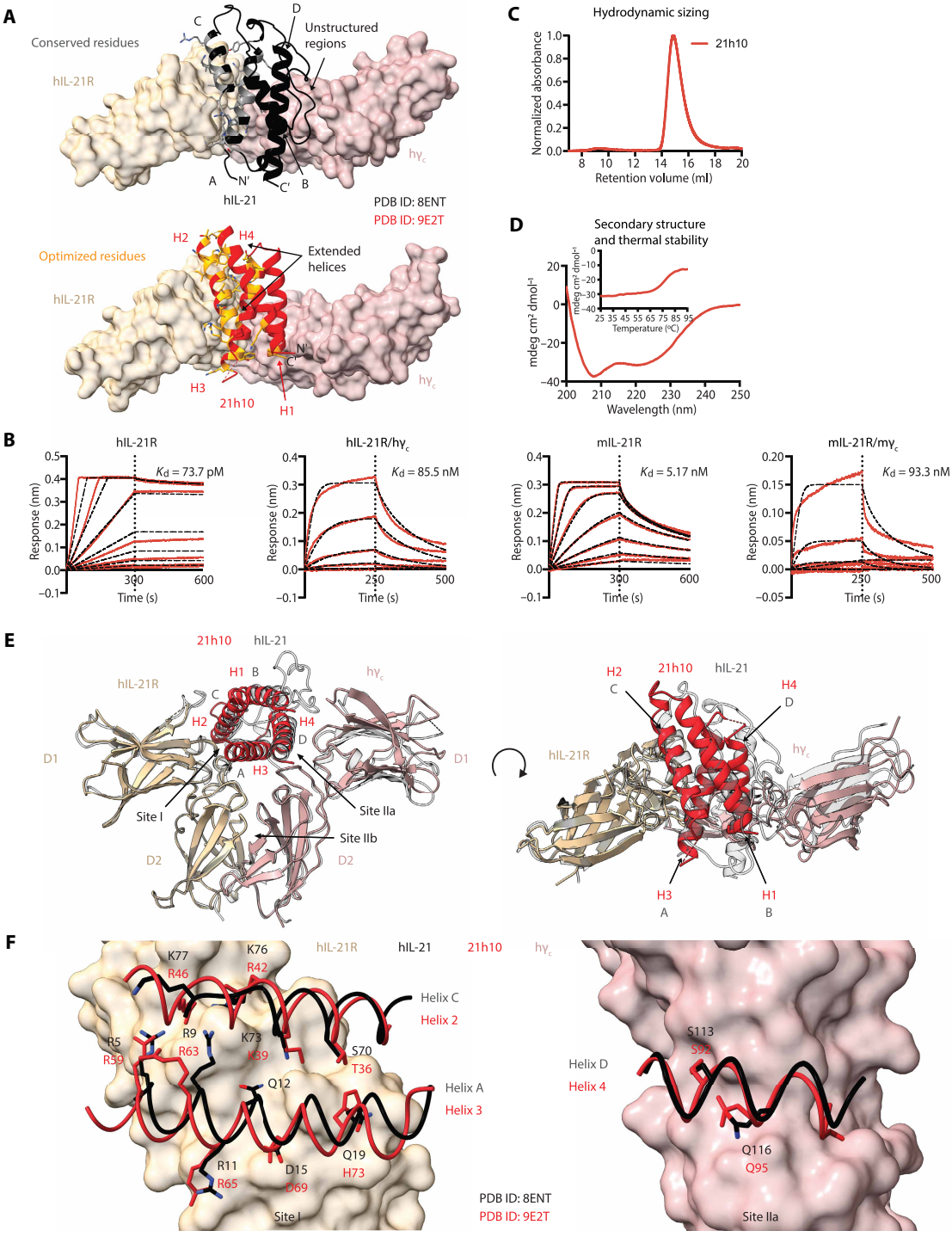

Fig. 1. A computationally designed IL-21 mimic recapitulates receptor interactions of native IL-21 with superior stability and human/murine cross-reactivity. (**A**) An optimized IL-21 mimic, 21h10, was designed by recapitulating the helical bundle structure of the native hIL-21. Unstructured regions in the hIL-21 were removed, and short helices were extended to accommodate improved intramolecular packing. Some of the interface residues are conserved from the native hIL-21 for the design of initial hits. Other residues from the de novo scaffolds are further optimized, as shown. The top panel is a top view of hIL-21 in complex with hIL-21R/hγ_c (PDB ID: 8ENT). The residues that were conserved during the initial design of the IL-21 mimic are colored in gray. The bottom panel is a top view of 21h10 in complex with hIL-21R/hγ_c (PDB ID: 9E2T) with the residues that were optimized colored in yellow. (**B**) Association and dissociation of 21h10 to human and mIL-21R and γ_c show concentration-dependent binding curves of 21h10. Black dotted lines show curve fits of raw data using the mass transport model. (**C**) Size exclusion chromatography of 21h10 using Superdex 75 10/300 GL column. (**D**) Wavelength scan from 200 to 250 nm for measuring α-helical secondary structure. Wavelength scan at 222 nm from 25° to 95°C for measuring thermal stability. (**E**) Crystal structure of 21h10 in complex with hIL-21R and hγ_c (PDB ID: 9E2T). (**F**) 21h10 conserves key molecular interactions in the site I interface (left) and site IIa interface (right) observed in the structure of the hIL-21 receptor complex (PDB ID: 8ENT).

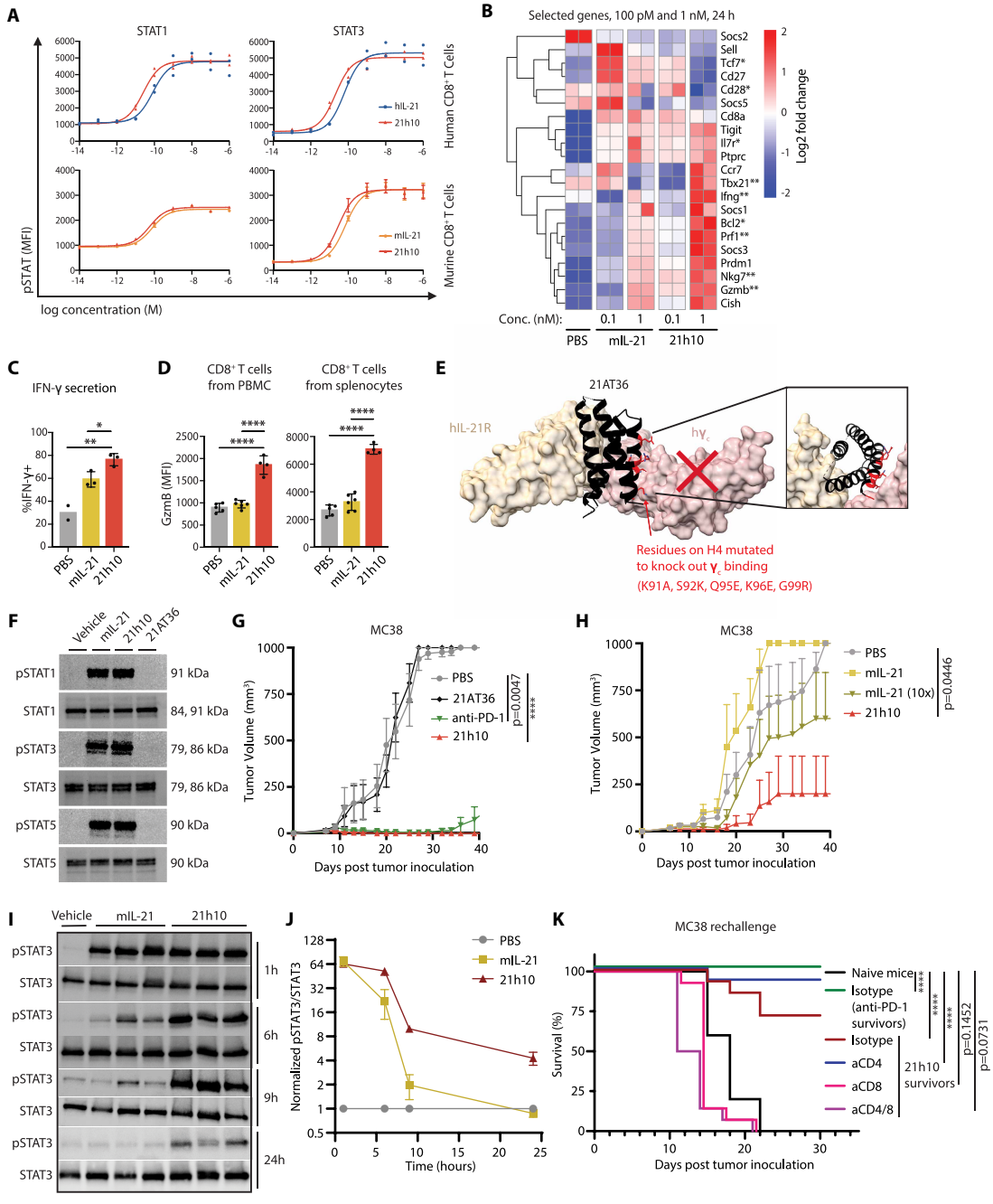

Fig. 2. 21h10 shows enhanced STAT signaling, gene expression, cellular phenotypes, and in vivo antitumor activity. (**A**) Human and murine CD8 T cells were treated with native IL-21 and 21h10 for 20 min (human, $n = 2$; murine, $n = 3$). (**B**) Genes related to cellular signaling and phenotype are compared for expression levels between murine CD8 T cells treated with PBS, mIL-21, or 21h10 at 100 pM or 1 nM ($n = 2$). Scale in log2 fold change. * and ** indicate memory-related and effector-related genes, respectively. After 24-hour treatment with the cytokines, cells were harvested for RNA-seq. (**C**) Percentage of murine IFN-γ^+ CD8 T cells upon treating with PBS, mIL-21, or 21h10 at 1 nM. Significance was determined using one-way ANOVA with Tukey's correction. (**D**) Granzyme B expression of LCMV-specific CD8 T cells from peripheral blood mononuclear cells (PBMCs) and splenocytes was measured 7 days after infection from LCMV-inoculated mice and daily injections of PBS, mIL-21 (2.5 μg), or 21h10 (2.5 μg) for 7 days. Significance was determined using lognormal one-way ANOVA with Tukey's multiple comparison test. (**E**) Computational model of 21AT36 with mutated residues highlighted in red. γ_c is illustrated to show the position of the removed γ_c interface. (**F**) Western blot for STAT and pSTAT with vehicle (PBS), mIL-21, 21h10, and 21AT36 in TRP1^{high} CD8 T cells. Representative of two experiments. (**G**) MC38-bearing mice were treated daily with PBS, 21AT36, 21h10, or anti–PD-1 for 14 days. Representative of three experiments. Significance was determined using Brown-Forsythe and Welch one-way ANOVA with Dunnett's correction using AUC values for each mouse versus PBS group. (**H**) Mice were inoculated with MC38 and treated with PBS, mIL-21, 10-fold dose mIL-21, and 21h10. Significance was determined using Brown-Forsythe and Welch ANOVA with Dunnett's correction using AUC values for each mouse. (**I**) Western blot for STAT3 and pSTAT3 in the spleens of mice treated with vehicle (PBS), mIL-21, and 21h10. Molecular weights of the bands are identical to those in (F). Representative of two experiments. (**J**) Normalized pSTAT3/STAT3 in spleens of treated mice over 24 hours from (I). (**K**) MC38 rechallenge of MC38 survivor mice from previous 21h10 or anti–PD-1 treatment. Significance was determined in Kaplan-Meier survival curves using Mantel-Cox log-rank tests comparing each group with the naive controls. MFI, mean fluorescence intensity.

maximal differentiation of murine CD8 T cells into $CD44^{+}CD62L^{-}$ effector T cells at 1 nM, whereas mIL-21 showed a similar effect at 100 nM (fig. S4D) accompanied by a robust increase in the secretion of interferon-γ (IFN-γ) at 1 nM (Fig. 2C). In mice infected with lymphocytic choriomeningitis virus (LCMV), daily intraperitoneal injection of 2.5 μg of 21h10 for 7 days induced granzyme B expression in virus-specific CD8 T cells in the peripheral blood and spleen harvested on day 7, whereas mIL-21 had minimal effects (Fig. 2D). Thus, 21h10 enhances effector CD8 T cell differentiation both in vitro and in vivo.

21h10 has potent antitumor activity in murine and human organotypic tumor models

Using ProteinMPNN (*43*), we redesigned the γ_c interface on helix H4 of 21h10 to abolish its receptor affinity, resulting in an antagonist, 21AT36, which binds to IL-21R but not γ_c (Fig. 2E, fig. S5A, and table S1). Whereas mIL-21 and 21h10 induced phosphorylation of STAT1, STAT3, and STAT5, 21AT36 did not induce STAT phosphorylation in murine CD8 T cells (Fig. 2F and fig. S5B). In mice bearing subcutaneous MC38 adenocarcinoma tumors (*44*), daily intraperitoneal treatment with 15 μg of 21h10 led to rapid tumor regression, similar to programmed cell death protein (PD)–1 blockade, whereas an equimolar dose of 21AT36, as expected, did not show antitumor activity (Fig. 2G and fig. S6A).

21h10 exhibited enhanced antitumor activity in the MC38 model compared with native IL-21 despite similar activity in cell culture, outperforming both a molar equivalent and a 10-fold molar excess of native IL-21 (Fig. 2H and fig. S7, A and B). We hypothesized that this increased activity was due to the enhanced stability of 21h10, resulting in resistance to serum proteases, longer receptor occupancy time, and prolonged in vivo signaling. To test this, we treated mice with a single intravenous dose of native mIL-21 or 21h10 and measured phosphorylated STAT3 (pSTAT3) in splenocytes over time. Despite similar initial levels of cytokine-induced pSTAT3, native mIL-21–induced pSTAT3 decreased rapidly with time, whereas 21h10-induced pSTAT3 declined more slowly and remained detectable at 24 hours after injection (Fig. 2, I to J). 21h10 also retained greater in vitro activity after incubation with murine serum compared with native mIL-21 (fig. S8A), consistent with the stronger phenotypic effects and slower binding reduction of 21h10 compared with native mIL-21 during prolonged in vitro incubation in serum-containing medium (figs. S4 and S8B).

The improved in vivo activity of 21h10 was not due to off-target binding, given that MC38 challenge in *Il21r*$^{-/-}$ mice showed no efficacy (fig. S6B). 21h10 treatment induced immune memory in mice that cleared MC38 tumors, given that animals rechallenged with MC38 tumors were protected. Memory responses were dependent on CD8 T cells, because protection was lost upon CD8 and CD8/CD4 T cell depletion, but not in animals depleted of CD4 T cells alone (Fig. 2K). In vitro, murine chimeric antigen receptor (CAR) T cells targeting human CD19 (hCD19) generated in the presence of 21h10 exhibited enhanced cell expansion and cytotoxicity against B16 melanoma cells engineered to express hCD19, with increased expression of CD25, granzyme B, and Bcl2 (fig. S9, A to C), a shift in cellular metabolism to a high metabolic state, and rapid elimination of MC38 adenocarcinoma when subjected to multiple rounds of tumor injection (fig. S9, D to F).

To determine the generalizability of our findings in MC38 adenocarcinoma, we assessed 21h10 in a less immunogenic tumor model. B16F10 is a model of poorly immunogenic melanoma known to respond to various immunotherapies, including cytokine therapies (*32*, *33*). Responses to B16F10 can be augmented through the transfer of tumor-specific CD8 T cells that recognize the tyrosinase-related protein 1 (TRP1) self-antigen with high or low affinity ($TRP1^{high}$ and $TRP1^{low}$ T cells, respectively), although these cells are insufficient to cause tumor regression on their own (*45*). Transferring $TRP1^{high}$ and $TRP1^{low}$ T cells models an oligoclonal T cell response to a tumor-associated self-antigen, analogous to what is observed in immunogenic human melanoma. We adoptively transferred $TRP1^{high/low}$ T cells and treated B16F10 melanoma-bearing mice with phosphate-buffered saline (PBS), mIL-21, or 21h10. mIL-21 treatment delayed tumor growth compared with PBS; however, as we observed for MC38, 21h10 treatment exhibited more robust tumor regression, with several long-term surviving animals (Fig. 3A and fig. S10A). Moreover, 21h10 synergized with adoptive cell transfer of $TRP1^{high/low}$ cells, as compared with no adoptive transfer, and 21h10 had stronger antitumor activity than was observed for the IL-2/IL-15 mimic Neo-2/15 (Fig. 3, B to C) (*32*, *33*). Strikingly, 21h10 treatment combined with adoptive T cell transfer resulted in complete tumor regression in 2 of the 13 animals (fig. S10, B to C). We found similarly enhanced B16F10 antitumor responses when 21h10 was combined with the antimelanoma antibody TA99 (fig. S11A) (*32*, *33*). Ex vivo treatment of $TRP1^{high/low}$ T cells with 21h10 for 2 days before transfer into B16F10-bearing mice only modestly decreased tumor growth (fig. S11B), suggesting that sustained signaling in the tumor microenvironment may be important for optimal antitumor (*46*, *47*) actions of 21h10.

To determine whether 21h10 had activity against human tumors, we used the patient-derived organotypic tumor spheroid (PDOTS) model (*48*, *49*). PDOTS, unlike organoids, are fresh tumor explants with an intact immune compartment for ex vivo profiling of the immunotherapy response in human tumors (*48*). PDOTS were derived from patients with advanced melanoma, with the majority of samples from patients who progressed on standard-of-care checkpoint blockade ($n = 11$ and $n = 9$ clinically resistant; table S7). 21h10 demonstrated activity against these resistant tumors, outperforming immune checkpoint blockade (ICB) antibodies (Fig. 3, D to G). These results indicate that human melanoma refractory to ICB contains T cells capable of being productively activated by 21h10.

21h10 induces nonneutralizing antidrug antibodies and toxicity that can be mitigated by TNF blockade

We next characterized the immunogenicity and tolerability of 21h10 in mice. Antidrug antibodies were detected in 5 of 30 mice treated with 21h10 in antitumor experiments, with low-titer antibodies to 21h10 detectable at a 1:100 dilution at a concentration two SDs above the mean of the PBS controls. No anti-21h10 antibodies were detected in mIL-21–treated or *Rag2*$^{-/-}$ controls (Fig. 4A), consistent with the low sequence homology between native mIL-21 and 21h10. Repeated cycles of dosing consisting of 9 days of 21h10 followed by at least 9 days of rest led to progressively higher incidence of antidrug antibodies detectable at 1:1000 dilution of serum (Fig. 4B). Mice with high titer antibodies did not develop injection site reactions or anaphylaxis, and all mice regained weight after each cycle of 21h10 dosing. Anti-21h10 antibodies did not appear to neutralize 21h10 given that 21h10 retained activity in these animals upon subsequent treatment for MC38 tumors. Mice that developed none, low-, or high-titer antibodies were able to subsequently respond to

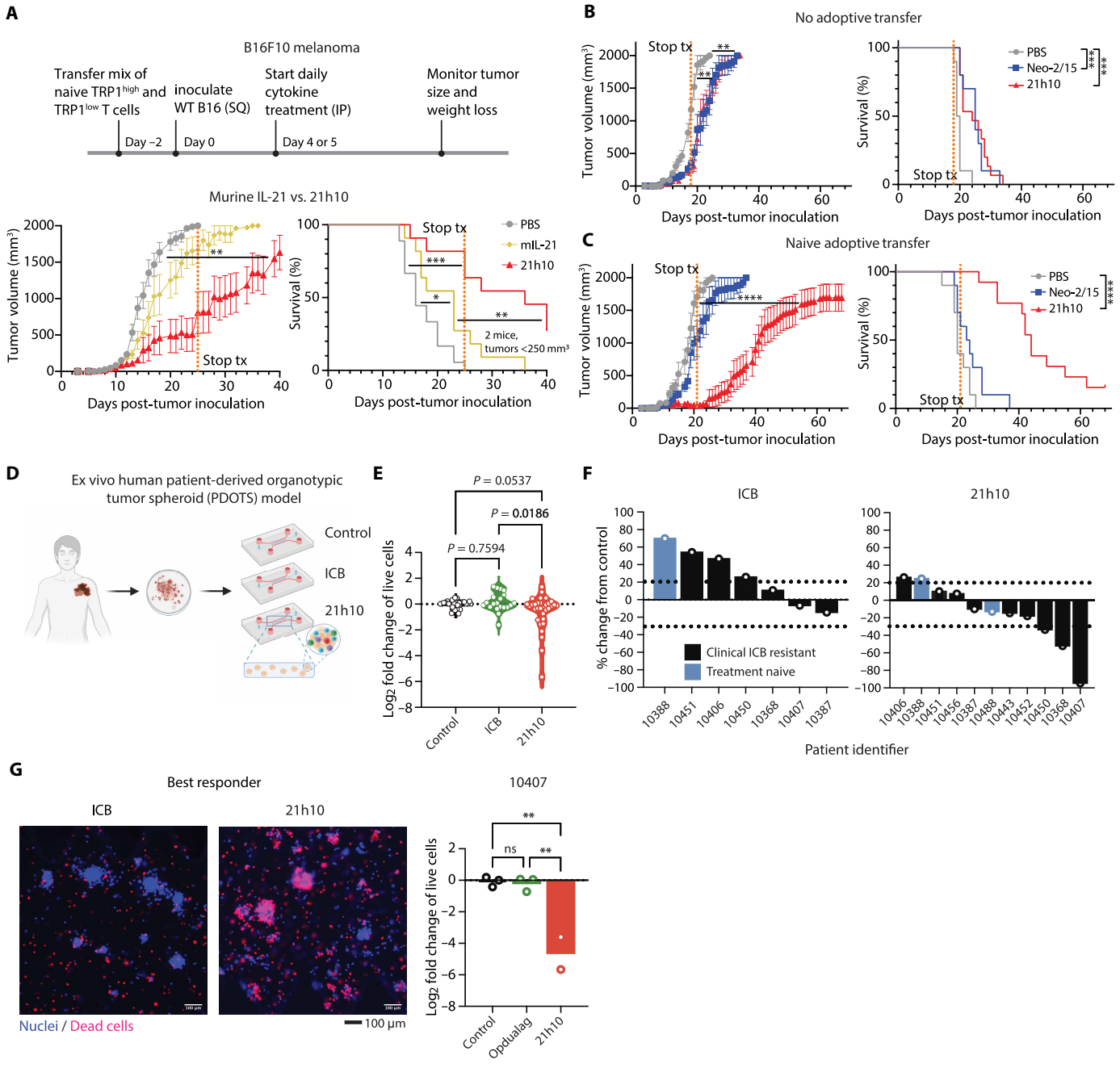

Fig. 3. 21h10 improves antitumor efficacy in in vivo B16F10 murine melanoma and ex vivo human PDOTS models. (**A**) Naïve CD8 TRP1$^{high/low}$ melanoma-specific T cells (5×10^5 cells) were adoptively transferred to mice before B16F10 inoculation. Cytokine therapy began on day 5 and continued every day until the end of treatment (dashed line). Figure created with BioRender. (**B**) Tumor volume in mice that received no prior T cell adoptive transfer before cytokine therapy. (**C**) Same as (B), but with adoptive transfer of naïve CD8 TRP1$^{high/low}$ T cells. For (A) to (C), significance was determined using Brown-Forsythe and Welch one-way ANOVA with Dunnett's correction using AUC values for each mouse versus PBS group. Significance was determined in Kaplan-Meier survival curves with Bonferroni-corrected Mantel-Cox log-rank tests. (**D**) Scheme of PDOTS preparation. Figure created with BioRender. (**E**) Microscopy-based viability assessment of ex vivo human melanoma PDOTS after treatment with ICB (anti–PD-1, pembrolizumab, or anti–PD-1 + anti–LAG-3), 21h10, or untreated control, showing aggregated data of 11 PDOTS with three technical repeats for each. Significance was determined using one-way ANOVA with Tukey's correction. (**F**) Viability assessment in (E) presented on a per-patient basis. The lower dashed line indicates tumor response (more than 30% reduction from control). The top dashed line indicates tumor growth (more than 20% elevation from control). (**G**) Representative images and viability assessment of the best responder PDOTS to 21h10 [patient 10407 in (F)]. Significance was determined using one-way ANOVA with Tukey's correction. PI-dead cells in red and Hoechst-nuclei in blue. IP, intraperitoneal.

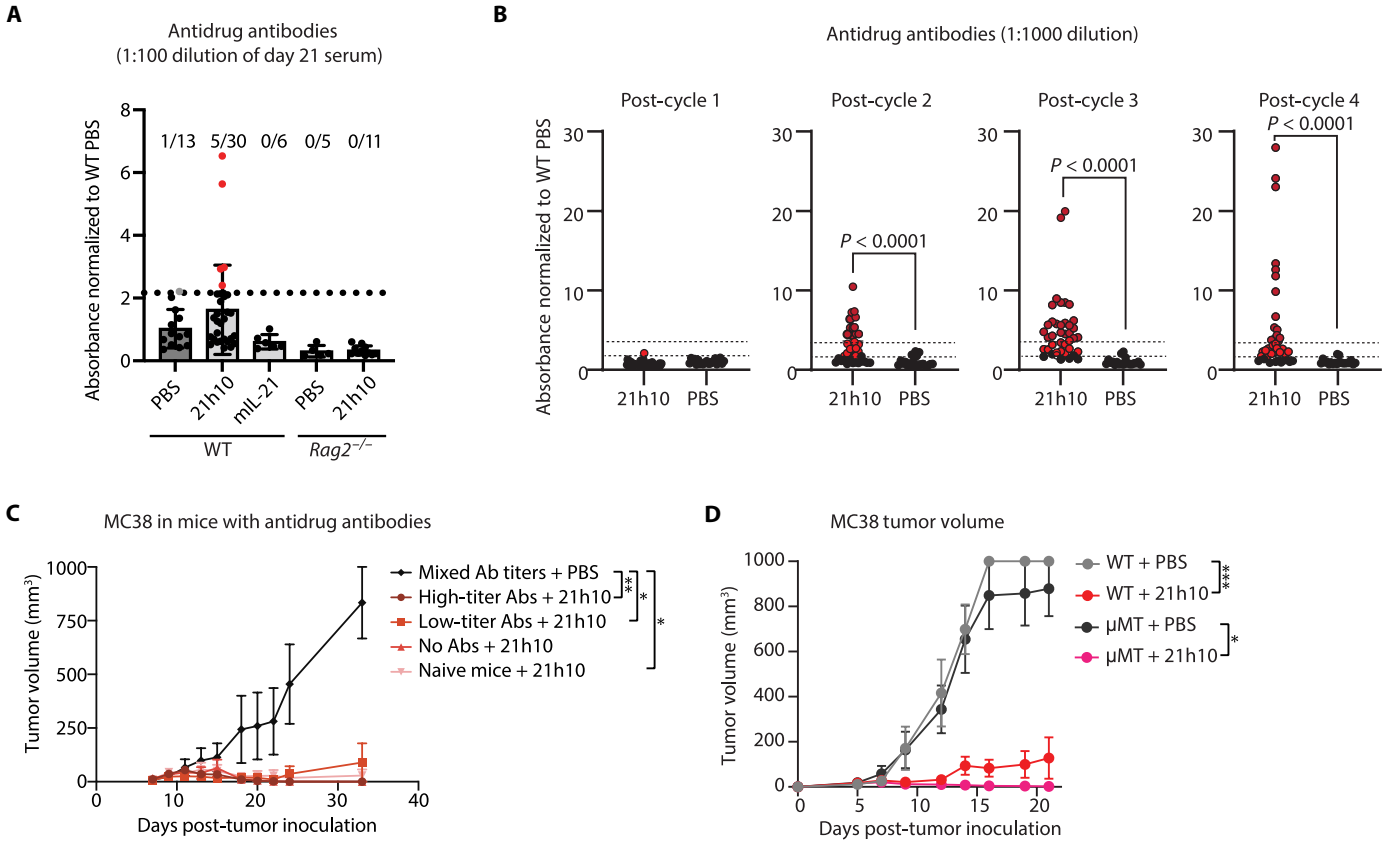

Fig. 4. 21h10 treatment elicits antidrug antibodies in mice. (**A**) Antidrug antibody titers were measured from day 21 sera of wild-type (WT) and *Rag2*$^{-/-}$ mice treated with PBS, 21h10 (15 μg), or mIL-21 (14.9 μg). (**B**) Antidrug antibody titers are measured from the sera of WT mice treated with multiple dosing cycles of 21h10 or PBS. Mice received daily 21h10 (15 μg) treatment for 9 days followed by at least 9 days of rest per cycle. Dashed lines indicate one or two SDs above the mean of the PBS controls and were used to define low-titer (one to two SDs above the mean, light red) and high-titer (greater than two SDs above the mean, dark red) serum samples. Significance was determined using Mann-Whitney test and reported when 21h10 was greater than the negative control. (**C**) Mice with various titer levels of anti-21h10 antibodies were inoculated with MC38 tumors. Starting on day 6, mice were treated with 21h10 or PBS daily for 17 days. Significance was determined using one-way ANOVA with Dunn's multiple comparisons correction using AUC values for each mouse versus the PBS group. (**D**) Antitumor activity of 21h10 in MC38 was compared in WT and μMT mice. Significance was determined using Brown-Forsythe and Welch one-way ANOVA with Dunnett's correction using AUC values for each mouse versus the PBS group.

21h10 treatment in the MC38 model, showing no correlation between antitumor activity and the level of anti-21h10 antibodies generated (Fig. 4C). Furthermore, the antitumor response against MC38 was not dependent on B cells, given that μMT mice, which lack B cells, showed responses to 21h10 that were equivalent to those of wild-type animals (Fig. 4D).

Although mice could tolerate 21h10 for 2 weeks of treatment, most animals exhibited weight loss with longer dosing. This toxicity did not require NK cells, because it was not attenuated by treatment with NK cell–depleting antibodies (Fig. 5A and fig. S12A). In contrast, *Rag2*$^{-/-}$ mice, which lack T and B cells, and *Rag2*$^{-/-}$ *Il2rg*$^{-/-}$ mice, which additionally lack NK cells and other innate lymphoid cells, were protected from 21h10 toxicity (Fig. 5A and fig. S12A), implicating adaptive immunity in 21h10 toxicity. To evaluate whether a cytokine produced by adaptive immune cells may be causing toxicity, we measured serum cytokines in 21h10-treated WT mice and *Rag2*$^{-/-}$ mice. Several cytokines were elevated in WT mice compared with *Rag2*$^{-/-}$ controls treated with 21h10 (Fig. 5, B and C), including TNF, which is known to contribute to immune-related toxicities in humans (*50*). When we coadministered an antibody that blocks TNF with 21h10, weight loss was mitigated, indicating that TNF plays an important role in 21h10 toxicity (Fig. 5D). The histological examination of mice treated with 21h10 revealed that most organs were normal (fig. S12B). We further evaluated serum creatinine, liver transaminases, and lung histology, which appeared similar to that in PBS-injected control mice (fig. S13). However, the exocrine pancreas was strikingly inflamed, with more than half of the pancreas area consisting of pancreatitis after 14 days of administration of 21h10 in WT but not in *Rag2*$^{-/-}$ mice (Fig. 5, E and F). Coadministration of TNF blockade greatly mitigated the development of pancreatitis, as shown by prevention of acinar-to-ductal metaplasia and lymphocytic infiltration (Fig. 5F). By multiple criteria, including histology, immunohistochemistry for tissue amylase, and serum amylase activity over time, TNF blockade reduced pancreatitis development from 21h10, making this a reasonable strategy for toxicity prevention (Fig. 5G). In the B16F10 melanoma model, the blockade of TNF did not impair the antitumor activity of 21h10, supporting successful prevention of toxicity and preservation of antitumor efficacy (Fig. 5H).

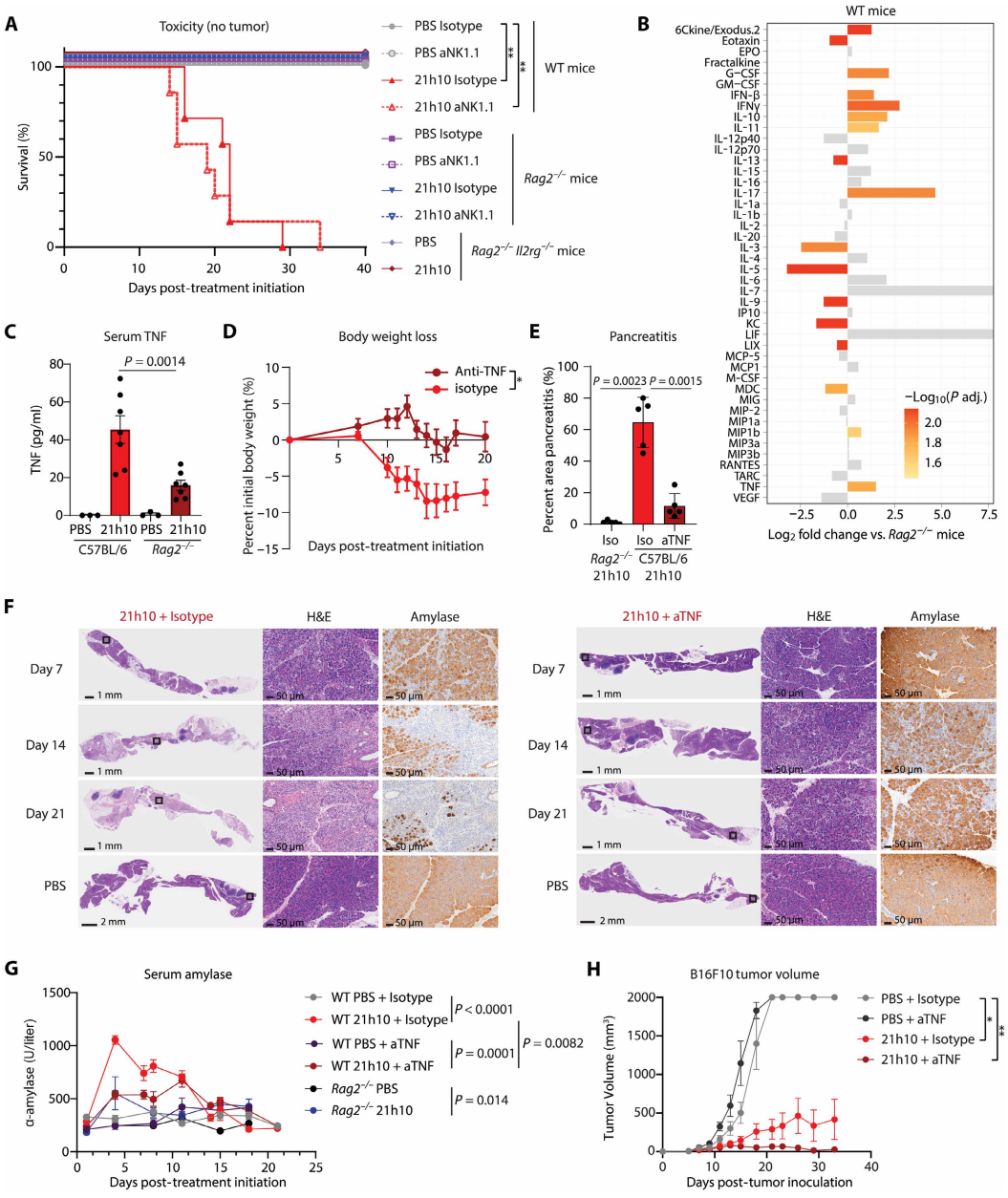

Fig. 5. Toxicity of 21h10 is alleviated by TNF blockade. (**A**) WT, *Rag2*$^{-/-}$, or *Rag2*$^{-/-}$ *Il2rg*$^{-/-}$ mice were treated with PBS or 21h10 daily and isotype or anti-NK1.1–depleting antibodies every 3 days. Mice were euthanized when weight loss exceeded 20% of the initial starting weight. Significance was determined in Kaplan-Meier survival curves with Bonferroni-corrected Mantel-Cox log-rank tests. (**B**) Serum cytokine levels of various cytokines after 21h10 treatment in WT mice in comparison with *Rag2*$^{-/-}$ mice. Bars in gray are nonsignificant compared with *Rag2*$^{-/-}$ mice. Adjusted *P* values were calculated from Wilcoxon tests with Bonferroni correction. (**C**) Serum TNF level was measured in C57BL/6 and *Rag2*$^{-/-}$ mice treated with PBS or 21h10. Significance was determined using one-way ANOVA with Šidák's correction. (**D**) Body weight change plot in isotype- and anti-TNF antibody–treated mice that received 21h10 treatment. Significance was determined using Mann-Whitney test of net AUC values for each mouse. (**E**) Percent area of pancreatitis in 21h10-treated *Rag2*$^{-/-}$ and C57BL/6 mice with isotype- or anti-TNF antibody treatments. Significance was determined using Brown-Forsythe and Welch ANOVA with Dunnett's correction. (**F**) Pancreas histology of mice treated with PBS, 21h10 + isotype antibody, or 21h10 + anti-TNF antibody on days 7, 14, and 21 from treatment initiation. Hematoxylin and eosin (H&E) and amylase stainings are shown on indicated days. (**G**) Serum amylase level was measured in WT mice treated with PBS + isotype antibody, 21h10 + isotype antibody, PBS + anti-TNF antibody, or 21h10 + anti-TNF antibody and in *Rag2*$^{-/-}$ mice treated with PBS or 21h10. Significance was determined using Brown-Forsythe and Welch ANOVA with Dunnett's correction using AUC values for each mouse. (**H**) Antitumor activity comparison on B16F10 melanoma between PBS + isotype antibody–, 21h10 + isotype antibody–, PBS + anti-TNF antibody–, and 21h10 + anti-TNF antibody–treated groups. Data are representative of two or three experiments. Significance was determined using Brown-Forsythe and Welch ANOVA with Dunnett's correction using AUC values for each mouse versus PBS + isotype group. G-CSF, granulocyte colony-stimulating factor; GM-CSF, granulocyte-macrophage colony-stimulating factor; EPO, erythropoietin; VEGF, vascular endothelial growth factor; LIF, leukemia inhibitory factor; LIX, lipopolysaccharide-induced CXC chemokine; MDC, monocyte-derived chemokine; M-CSF, macrophage colony-stimulating factor; MCP1, monocyte chemoattractant protein 1; MIG, monokine induced by gamma interferon; KC, keratinocyte-derived chemokine; RANTES, regulated on activation, normal T cell expressed and secreted; TARC, thymus and activation regulated chemokine.

21h10 expands tumor cytotoxic T cells and reduces T_{reg} cell infiltration

IL-21 has diverse roles within the immune system depending on the responding cells and the context in which it is produced (*10*). To understand the mechanism of action of 21h10, we performed single-cell RNA sequencing (scRNAseq) on $CD45^+$ enriched cells from B16F10 melanoma tumors 14 days after tumor inoculation, comparing mice treated with PBS, Neo-2/15, mIL-21, and 21h10 in addition to adoptively transferred $TRP1^{high/low}$ CD8 T cells. Using unbiased clustering, we identified populations of T cells, multiple monocyte/macrophage populations, dendritic cells, and smaller clusters of B cells, NK cells, granulocytes, melanoma cells, and fibroblasts (Fig. 6A and fig. S14A) in each treatment group (Fig. 6B). All T cell clusters were expanded in mice treated with Neo-2/15 (Fig. 6, B and C), consistent with the known effects of IL-2 and IL-2 mimics on T cell proliferation and survival (*51*). Conversely, 21h10, mIL-21, and PBS had modest effects on the relative proportion of T cells within the tumor microenvironment (Fig. 6, B and C). The T cell expansion observed with Neo-2/15 was primarily among CD8 T cells, consistent with preferential expansion of CD8 T cells compared with CD4 T cells by IL-2 (Fig. 6D and fig. S15A) (*52*). Similar to total T cells, TRP1-specific T cells, particularly low-affinity $TRP1^{low}$ cells, expanded with Neo-2/15 (Fig. 6E). Although 21h10 treatment did not expand total CD8 T cells, tumor-specific low-affinity $TRP1^{low}$ cells accumulated in 21h10-treated tumors (Fig. 6E), consistent with studies showing that low-affinity T cell expansion can be greater than that of their high-affinity counterparts (*53*). Native mIL-21 did not expand $TRP1^{high}$ or $TRP1^{low}$ T cells (Fig. 6E).

The high antitumor activity of 21h10 is notable, given the modest effect on T cell expansion. T cell subclustering identified two naïve T cell populations expressing *Tcf7*, a migratory cluster (*Itga4* and *Themis*), activated CD8 T cells (*Ccl5* and *Gzmk*), highly activated CD8 T cells expressing multiple immune checkpoint receptors (*Havcr2* and *Lag3*) and effector molecules (*Gzmb* and *Ifng*), a proliferative cluster (*Mki67* and *Birc5*) and CD4 T cells (*Cd4* and *Cd40lg*), regulatory T (T_{reg}) cells (*Foxp3* and *Ctla4*), and γδ T cell clusters (Fig. 6F and fig. S14B). T cell expansion by Neo-2/15 mainly occurred in the migratory and cycling clusters, but 21h10 had a greater effect on highly activated CD8 T cells. No significant increases in specific T cell populations were observed with mIL-21. Neo-2/15 primarily affected pathways involved in cell growth and proliferation, whereas mIL-21 showed a similar, albeit weaker effect compared with PBS. 21h10 treatment was associated with IFN-γ/IFN-α response genes and growth pathways (fig. S14C) in all immune populations identified, including the myeloid and T cell clusters (Fig. 6G). 21h10 expanded the most activated CD8 T cells and increased *Ifng* and *Gzmb* gene expression in most T cell subclusters (Fig. 6H), including the transferred melanoma-specific CD8 T cells (Fig. 6I). Correspondingly, IFN-γ and granzyme B levels were increased in both endogenous and transferred T cells from 21h10-treated animals, as compared with PBS controls (Fig. 6J and fig. S15B). Increases in *Gzmb* and *Prf1* were also observed in NK cells from mice treated with 21h10, although total NK cell frequencies were similar between PBS and 21h10 groups (fig. S14, D and E).

There were fewer tumor-infiltrating CD4 T cells than CD8 T cells, as shown by both flow cytometry and scRNAseq (Fig. 6, C and D). We subclustered the CD4 T cells in our scRNAseq data and identified four populations: naïve CD4, cycling CD4 T cells, T_{reg} cells, and T helper 1 (T_H1) cells expressing *Ifng* mRNA (Fig. 6K and fig. S14F). The $Ifng^+$ T_H1 cells preferentially expanded in response to 21h10 as compared with the other treatments and had higher levels of IL-21R, analogous to what we observed with CD8 T cells (Fig. 6, K and L, and figs. S15C and S16). Our scRNAseq analysis also suggested that 21h10 decreased T_{reg} cells, which we confirmed by flow cytometry using Foxp3–green fluorescent protein (GFP) reporter mice (Fig. 6M). Thus, 21h10 treatment robustly activates STAT1 and STAT3 in T cells in the tumor microenvironment, and this is accompanied by a shift toward highly activated, IFN-γ– and granzyme-B–producing, antimelanoma CD8 T cells and a relative increase in T_H1 cells and decrease in T_{reg} cells.

DISCUSSION

Cytokine-based therapies for cancer have historically had limited efficacy and high toxicity (*54*–*56*). Here, we show that a computationally designed mimic of IL-21 with improved stability can have potent antitumor activity, both as a monotherapy and in combination with adoptive T cell therapies. 21h10 expanded highly activated effector CD8 T cells in the tumor microenvironment, with the effect most pronounced for CD8 T cells with known tumor reactivity. In contrast, the IL-2/IL-15 mimic Neo-2/15 expanded multiple T cell populations without a preferential effect on the differentiation of effector cells, providing a possible mechanistic explanation for the difference in antitumor activity between these two cytokine mimics. Antitumor T cell responses can display a range of receptor affinities, with low-affinity responses typically seen when a self-antigen is targeted (*57*, *58*). Using scRNA-seq, we found that CD8 T cells recognizing the melanoma self-antigen TRP1 with a range of affinities were expanded by 21h10, but strikingly, low-affinity TRP1-specific T cells were preferentially increased, indicating that 21h10 selectively amplified lower affinity antitumor T cells. By contrast, programmed cell death protein 1 (PD-1) blockade immunotherapies appear to act on high-affinity neoantigen-reactive clonotypes (*59*), and immunotherapies that can augment a broader spectrum of TCR affinities are currently lacking. Low-affinity T cells often fail to receive a signal strong enough to overcome the TCR signaling threshold (*60*) and thus are frequently unable to contribute to antitumor immunity (*45*). By expanding the $TRP1^{low}$ population, 21h10 broadens the repertoire of the antitumor immune response, potentially explaining the efficacy observed in ex vivo cultures of immunotherapy-resistant human melanoma. 21h10 also decreased the T_{reg} cell population while inducing an effector phenotype on CD8 T cells. Although IL-21 has important roles in B cell differentiation, class switching, and NK cell activation, neither B nor NK cells were significantly altered in our in vivo tumor models.

Although we chose 21h10 for its ability to mimic IL-21 signaling in vitro, the resulting de novo protein exhibited substantially superior performance in vivo. 21h10 has increased serum stability compared with native mIL-21, leading to sustained potency in vivo. The increase in the duration of signaling in vivo leads to enhanced phenotypic changes and, ultimately, improved antitumor responses. These improvements highlight the robustness of de novo protein design approaches for developing therapeutic candidates with improved properties. The full human/murine cross-reactivity and engineerability of 21h10 should make it straightforward to generate targeted and conditionally active versions (*33*) to mitigate toxicity and target activity to the tumor microenvironment.

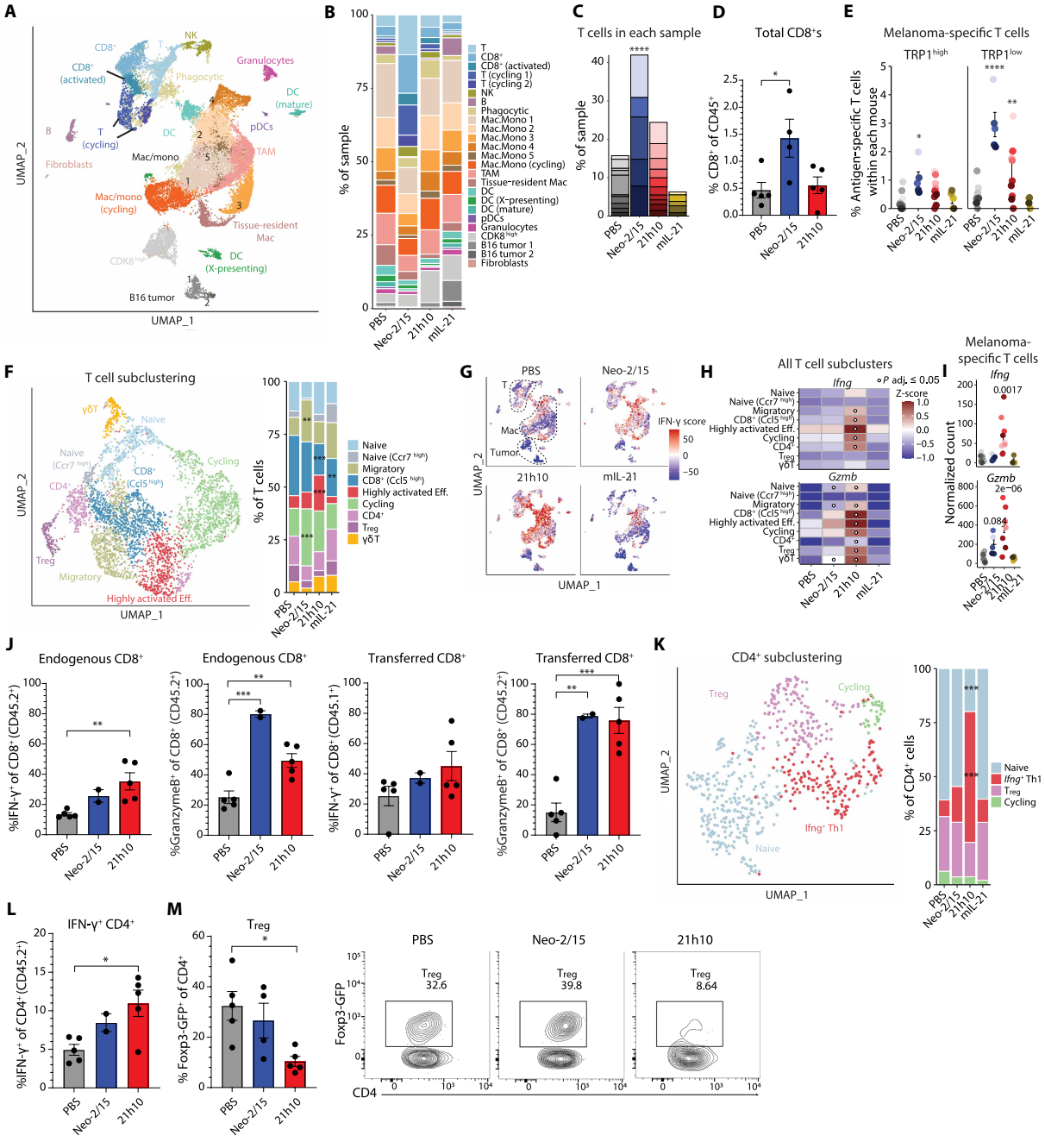

Fig. 6. 21h10 treatment results in expanded antitumor T cells with enhanced effector phenotype. (**A**) Mice were treated as in Fig. 3 (A and C), but on day 15 of tumor growth, tumors were processed for scRNAseq. Ten (PBS, 21h10) or five (Neo-2/15, mIL-21) mice per group were collected, and individual tumors were labeled with hashtag antibodies before pooling tumors from each group and sequencing. UMAP of all samples are combined. (**B**) scRNAseq cluster composition average across treatment groups. (**C**) T cells in each scRNAseq sample from (B). Different colors for each bar indicate individual mice from each group. Significance was determined using one-way ANOVA with Dunnett's multiple comparisons. (**D**) Flow cytometry quantification of CD8 T cell infiltration. Significance was determined using one-way ANOVA with Dunnett's multiple comparisons. (**E**) TRP1^{high} and TRP1^{low} melanoma antigen-specific cells captured by sequencing. Significance compared with the PBS group was determined using two-way ANOVA with Dunnett's multiple comparisons. (**F**) T cells were subclustered from all samples from (A). The average T cell subcluster composition across treatment groups is shown on the right. Significance compared with the PBS group was determined using two-way ANOVA with Dunnett's multiple comparisons. (**G**) IFN-γ response score total UMAP from (A) based on scaled and summed Hallmark IFN-γ response genes for each cell. (**H**) Heatmap from pseudo-bulk differential gene expression analysis across T cell subclusters. Significant differences compared with the PBS groups. (**I**) Similar to (H), but for TRP1 cells only; values from individual mice are shown. Adjusted *P* values displayed versus PBS samples. (**J**) Flow cytometry quantification of CD8 IFN-γ/granzyme B levels in endogenous or transferred CD8 TRP1$^{high/low}$ T cells. (**K**) CD4 T cell subclustering UMAP and cluster composition. Significance compared with the PBS group was determined using two-way ANOVA with Dunnett's multiple comparisons. (**L**) Flow cytometry of IFN-γ$^+$ CD4 T cells. (**M**) Quantification and representative flow cytometry plots of Foxp3-GFP T_{reg} cells. Significance was determined using one-way ANOVA with Dunnett's multiple comparisons for flow cytometry quantification and scRNA-seq total T cell comparison. DESeq2 was used to identify differentially expressed genes from scRNA-seq using the Wald test. For all dot plots with error bars, dots indicate individual mice, and bars indicate SEM.

Limitations to clinical development of 21h10 include toxicity, a concern for any systemically delivered cytokine, and immunogenicity, a concern for any de novo protein intended to be administered more than once. We used 21h10 as an example to address both of these broader issues. Toxicity appeared to be associated with a specific organ (the pancreas) and mediated by TNF, which could be prevented by TNF blockade, a therapy commonly used for treatment of immune-related adverse events (*61*). Use of a two-drug regimen could be clinically challenging; thus, the further design of 21h10 might include fusion with targeting domains to avoid accumulation in the pancreas or fusion with a designed protein that blocks TNF signaling. Immunization with 21h10 led to formation of antidrug antibodies, but they were not neutralizing and did not attenuate the therapeutic efficacy of 21h10 in our models. Similarly, antidrug antibodies to the designed cytokine Neo-2/15 were rare and did not attenuate efficacy, as we previously reported (*32*). We hypothesize that either the immunodominant epitopes for these two examples of cytokine mimics are not located in the receptor binding interface or that the high affinity of 21h10 for its receptor allows binding even in the presence of a bound antibody. Although the placement of the immunodominant epitopes or affinity of the elicited antibodies appears to have fortuitously worked in our favor, efforts to intentionally redirect antidrug antibodies away from receptor binding interfaces may be important in the design of future cytokine mimics.

In summary, we have developed a potent IL-21 mimic with activity on both human and murine cells that exhibits robust antitumor activity in multiple tumor models. 21h10 has antitumor activity as a monotherapy, synergizes with adoptive cell therapy in a B16F10 melanoma model, and is curative in a highly immunogenic MC38 adenocarcinoma model. 21h10 causes pancreatitis in mice, but it is mitigated by TNF blockade. The activity of 21h10 in human refractory melanoma PDOTS and its superiority to clinically approved ICB treatments suggest the potential for clinical translation to treat tumors unresponsive to checkpoint blockade and other existing therapies.

MATERIALS AND METHODS

Study design

This study aimed to evaluate the stability, signaling activity, immunogenicity, toxicity, and antitumor efficacy of 21h10, a computationally designed de novo mimic of IL-21, in both murine models and ex vivo human tumor explants. The study involved in vitro biochemical and signaling assays, murine tumor models (MC38 and B16F10), adoptive T cell transfer, CAR T cells, PDOTS, and scRNA-seq to characterize immune responses. Sample sizes were determined on the basis of prior experiments and effect size expectations in similar models, although formal power calculations were not performed. No animals or data points were excluded unless pre-established technical failure criteria (e.g., injection errors and lack of tumor engraftment) were met.

Randomization was performed for animal studies where mice were randomly assigned to treatment groups once tumors reached comparable sizes. Human tumor explants were allocated on the basis of tissue availability, and the researchers were not blinded to the treatment conditions. Blinding was implemented for outcome assessments where feasible, including for tumor measurements, immunohistochemistry, and histological scoring of toxicity. Experiments were conducted in multiple independent biological replicates: Tumor treatment studies were repeated at least twice with 5 to 10 animals per group, and PDOTS experiments were performed using 11 patient samples, with two or three biological replicates for each. Flow cytometry, RNA-seq, and scRNA-seq experiments were conducted with independent replicates from separate tissue preparations or donors. Specific details on replicates and statistical methods are provided in the respective figure legends and data file S1.

Computational design of de novo IL-21 mimic

The crystal structure of hIL-21 with hIL-21R [Protein Data Bank (PDB): 3TGX] was used to design the mimics of native IL-21. The *PyRosetta* script with PDBInfoLabel metadata implementation generated IL-21–like scaffolds (*32*) in code S1. The residues from the hIL-21 are designated to be fixed during scaffold generation and interface residue design in code S2. The nonfixed residues were designed using *Rosetta* FastDesign and relaxed using *Rosetta* FastRelax with the "beta_nov16" score function. Designs (185) were filtered with *Rosetta* score metrics: packstat of > 0.6, score_per_residue of < -2.3, and sspred of > 0.8.

Crystallization, data collection, and refinement

hIL-21R and hγ_c were expressed, purified, and deglycosylated as previously described (*37*). hγ_c was mixed with 21h10/hIL-21R complex at an equimolar ratio, concentrated to 10 mg/ml, and treated with carboxypeptidase A and B. Crystals of the 21h10 complex were grown by sitting drop vapor diffusion in 0.2 M potassium thiocyanate, 0.1 M bis-tris propane (pH 6.5); 20% (w/v) polyethylene glycol, molecular weight 3350; and crystals were harvested as previously described. Diffraction data were collected at Stanford Synchrotron Radiation Laboratory beamline 12-2. Data were indexed, integrated, and scaled to 2.3-Å resolution using XDS (*62*). Because of anisotropy in the crystal diffraction, a pseudoellipsoidal diffraction limit was applied using Staraniso (*63*). The protein structure was solved using an approach similar to the solution of the native ternary structure (*37*) using molecular replacement in Phaser (*64*) based on models derived from the hIL-21/hIL-21R complex (PDB: 3TGX) (*35*) and a hγ_c complex (PDB: 7S2R) (*65*). The solution yielded an asymmetric unit containing four copies of 21h10, four copies of hIL-21R, and two copies of hγ_c. Coot (*66*) and Phenix (*67*) were used to rebuild and refine the structure, and refinement was performed with noncrystallographic symmetry restraints. Crystallography data collection and refinement statistics are presented in table S3. The final 21h10/hIL-21/hIL-21R structure has been deposited in the RCSB protein data bank with accession code PDB ID: 9E2T. SBGrid (*68*) was used to install and configure all crystallographic software. The analysis of interfaces was conducted using Protein Interfaces, Surfaces and Assemblies (PISA) (table S4) (*69*). Structure-related figures were generated using UCSF ChimeraX (*70*).

STAT phosphorylation assay in T cells

All experiments involving mice at NHLBI were performed using protocols approved by the NHLBI Animal Care and Use Committee and followed National Institutes of Health (NIH) guidelines for the use of animals in intramural research. Purified murine CD4 and CD8 T cells were preactivated with plate-bound anti-murine CD3 (2 μg/ml; clone 145-2C11, Bio X Cell, catalog no. BE0001-1) and soluble anti-murine CD28 (1 μg/ml; clone 37.51, Bio X Cell, catalog no. BE0015-1) and cultured in complete RPMI medium for 48 hours at 37°C. Human CD4 and CD8 T cells were isolated from the buffy coats of healthy human volunteers obtained from NIH Blood Bank. Purified human

CD4 and CD8 T cells were activated by plate-bound anti-human CD3 (2 μg/ml; clone UCHT1 (Leu-4) (T3), Bio X Cell, catalog no. BE0231) and soluble anti-human CD28 (1 μg/ml; clone 9.3, Bio X Cell, catalog no. BE0248) and cultured in complete RPMI medium for 48 hours at 37°C. For B cells, see Supplementary Materials and Methods for details.

After 48 hours of culture, the preactivated cells were rested overnight in a complete medium and restimulated with native IL-21 and IL-21 mimics at different concentrations (from 10 fM to 1 μM) for 20 min, respectively. Cells were then fixed, permeabilized, and stained with AF488-phosphoSTAT1 (1:100; BD Biosciences, catalog no. 612-596) and AF647-phosphoSTAT3 (1:100; BD Biosciences, catalog no. 651008) for flow cytometry. Cells were analyzed using a BD LSR Fortessa X-20 Cell Analyzer flow cytometer (BD Biosciences).

RNA-seq analysis

The libraries were indexed using barcodes and sequenced on an Illumina NovaSeq platform with SP 100-cycle kits, achieving a sequencing depth of more than 45 million reads per sample. Sequenced reads were obtained with the Illumina CASAVA pipeline and mapped to the murine genome (mm10/GRCm38) using TopHat 2.0.11. Raw counts that fell on exons of each gene were calculated and normalized by using RPKM (reads per kilobase per million mapped reads). Differentially expressed genes were identified with the R Bioconductor package "edgeR," and expression heatmaps were generated with the R package "pheatmap."

Syngeneic murine tumor model experiments

All animal protocols were approved by the Dana-Farber Cancer Institute Committee on Animal Care (protocol 14-019 and 14-037) and are in compliance with the NIH/NCI ethical guidelines for tumor-bearing animals. On day 0, 6- to 8-week-old female C57BL/6J mice (the Jackson Laboratory, catalog no. 000664) were inoculated with 80 to 90% confluent tumor cells (cell line is indicated per experiment). Starting on days 3 to 5, mice were treated daily with the listed test items, and 21h10 was injected daily following each regimen indicated per experiment. Mice were monitored for survival, weight change, and symptoms of toxicity, including pallor, noticeable weight loss, and fatigue. Mice were euthanized if they lost 20% of body weight or their tumors ulcerated or reached 2000 mm^3 in volume (measured with a ruler, volume calculated by multiplication of length, height, and width), which is the maximal permitted tumor size for these studies. For all in vivo murine tumor experiments, mice were randomized after transfer of TRP1 cells and after inoculation of tumors, before starting drug treatment. Mice that did not have palpable tumors at the time of first drug dosing were excluded from the experiment. Mice whose tumors ulcerated before reaching 500 mm^3 were also excluded. Investigators were not blinded. Sample size determination was not performed.

PDOTS preparation and microfluidic device culture

Organotypic spheroids were generated from samples of patients with melanoma at Massachusetts General Hospital. Samples were collected and analyzed according to Dana-Farber/Harvard Cancer Center Institutional Review Board (IRB)–approved protocols (IRB protocol: 11-181). Written informed consent was obtained from all patients. PDOTS were generated as previously described (*48*, *71*, *72*). Tumors were minced finely with scalples. Minced tumors were resuspended in full Dulbecco's modified Eagle's medium. Cells were filtered through 100-μm cell strainer, followed by 40-μm cell strainer to obtain three size-based fractions: S1 (>100 μm), S2 (40 to 100 μm), and S3 (<40 μm). The S2 and S3 fractions were washed off the filters with fresh complete medium and rested in ultralow attachment plates (Corning, 3471) in the incubator until device loading. The S1 fraction was washed off using a complete medium supplemented with collagenase type IV (100 U/ml; Life Technologies, 17104019) and 15 mM Hepes (Gibco, 1560-080), followed by incubation at 37°C for 15 to 30 min. Collagen digestion was quenched with an equal volume of medium, and the suspension was subsequently refiltered to S1, S2, and S3 fractions. S1 was washed off this time with complete medium. Last, the S2 fraction was pelleted and embedded in type I rat tail collagen (Corning, 354236) at 2.5 mg/ml, prepared with 10× PBS containing phenol red (Sigma-Aldrich, 114537-5g). PDOTS was treated with ICB [pembrolizumab (250 μg/ml) or nivolumab (240 μg/ml) + relatlimab (80 μg/ml) (opdualag, obtained from MGH pharmacy waste)] human recombinant IL-21 at 1 μM or left untreated.

PDOTS viability assessment

PDOTS staining and viability analysis was done as previously described (*48*, *71*). Image analysis was performed using the NIS-Elements AR software. Live/dead quantification was determined by measuring the total cell area of acridine orange (live cells), propidium iodide (PI; dead cells), and Hoechst (total cells). Live cell counts were defined as the total area of the acridine orange channel or as the Hoechst (total cell counts) minus the PI (dead) area. Percent change and $\log_2$-fold change (L2FC) values were calculated from the live cells in each condition relative to the control.

scRNA-seq preparation

Tumors were collected from mice as described previously (*73*). For each tumor from a treatment group, a different TotalSeqC hashing antibody (mouse Hashtags 1-5, BioLegend) was incubated with 2 μl of antibody/million cells in PBS (with 2% fetal bovine serum) for 20 min at 4°C. About 4000 cells per tumor were pooled across each treatment group (five hashtags per treatment group) and loaded onto a 10X Chromium Controller with a Single Cell K Chip (PN-2000182) using the Chromium Next GEM Single Cell 5′ GEM Kit v2 reagents and beads (PN-1000244 and PN-1000264). Samples were sequenced at a depth of 50,000 read pairs per cell.

scRNA-seq preprocessing

The *Mus musculus* genome fasta and general transfer format (GTF) annotation files were downloaded from the Ensembl database (release 108). CellRanger (v7.0.0) "mkgtf" was used to filter the GTF file using the defaults from 10x Genomics. A custom reference was generated by first appending the sequences for the $TRP1^{high/low}$ rearranged α/β TCR chains (*45*) to the *M. musculus* fasta file, adding TRP1 TCR annotations to the filtered GTF file, and last using these two new files as inputs for CellRanger "mkref" to build the reference. Cellranger "count" was used to align reads to this new reference (Gene Expression) and hashtag antibody sequences (antibody capture). The unfiltered CellRanger count matrices were imported into R using the Seurat (v4.3.0) package. The DropletUtils (v1.18.1) package "emptyDrops" function was used to exclude potential empty droplets from the count matrix (*74*) using a cutoff of false discovery rate < 0.01. Hashtag reads were used to demultiplex samples with the Seurat "HTODemux" function using a kmeans function with "nstarts = 30" and a 99% positive quantile threshold.

scRNA-seq clustering

Each filtered, demultiplexed sample was log-normalized, and 2000 variable features were identified and used to find 3000 integration features to combine samples to minimize batch effects (*75*). The newly integrated dataset was scaled, and a principal components analysis was performed, from which the top 25 PCs were used for uniform manifold approximation and projection (UMAP) generation. From the 25 PCs, a shared nearest neighbor graph was constructed ($k = 20$ neighbors), and clusters were classified by the Louvain algorithm. The "FindAllMarkers" function was used to find the top cluster-defining genes, and these gene lists were used to assign cell types.

Differential gene expression analysis

Across each T cell subcluster, we performed a pseudo-bulk method of differential gene expression analysis (*76*, *77*). Each mouse within a treatment group was treated as a replicate, and count matrices were summed across genes for each subcluster per mouse. Using the DESeq2 (v1.38.3) package (*78*) and pseudo-bulk gene expression values, differentially expressed genes were identified across treatment groups and subclusters. For gene changes in TRP1-specific T cells, cells classified as either $TRP1^{high}$ or $TRP1^{low}$ cells were subset, and counts across each gene were summed for each mouse for pseudo-bulk analysis using DESeq2. For Gene Set Enrichment Analysis (GSEA), fold changes within the T cell subset object were calculated with the Seurat "FoldChange" function, comparing each specified treatment group. Fold changes were used with the fgsea (v1.24.0) package along with the Molecular Signatures (v7.2) Hallmark gene signatures (*79*) for GSEA.

Statistical analysis

Statistical comparisons were made using GraphPad Prism 10 (GraphPad Software) or R (v4.2.2), and details are reported in data file S1. Parametric comparisons of normally distributed values were performed using one-way or two-way analysis of variance (ANOVA) with appropriate corrections for multiple comparisons, including Tukey's, Dunnett's, and Šidák corrections, as specified. In cases of unequal variances, Brown-Forsythe and Welch ANOVA tests were used with Dunnett's multiple comparisons correction. For survival analyses, significance was determined using Bonferroni-adjusted Mantel-Cox log-rank tests. Where applicable, Mann-Whitney *U* tests were used for nonparametric unpaired comparisons, and Wilcoxon signed-rank tests with Bonferroni correction were applied to paired data. Area under the curve (AUC) values per mouse were used in some group comparisons. For gene expression and enrichment analyses, DESeq2 Wald tests and the fgsea R package were used using an adjusted *P* value cutoff of 0.05. *z* scores were computed by subtracting the row mean from each value and dividing by the row standard deviation. All statistical tests were two-tailed, and adjustments for multiple comparisons were made where appropriate. All error bars are SEM. Data were considered significant when $P \leq 0.05$; $*P < 0.05$, $**P < 0.01$, $***P < 0.001$, and $****P < 0.0001$ (or *P* values displayed).

Supplementary Materials

The PDF file includes:
Materials and Methods
Figs. S1 to S16
Tables S1 to S7
Codes S1 and S2
References (*80*, *81*)

Other Supplementary Material for this manuscript includes the following:
Data files S1 to S3
MDAR Reproducibility Checklist

REFERENCES AND NOTES

1. R. Spolski, W. J. Leonard, Interleukin-21: Basic biology and implications for cancer and autoimmunity. *Annu. Rev. Immunol.* **26**, 57–79 (2008).
2. W. J. Leonard, R. Spolski, Interleukin-21: A modulator of lymphoid proliferation, apoptosis and differentiation. *Nat. Rev. Immunol.* **5**, 688–698 (2005).
3. M. T. Kasaian, M. J. Whitters, L. L. Carter, L. D. Lowe, J. M. Jussif, B. Deng, K. A. Johnson, J. S. Witek, M. Senices, R. F. Konz, A. L. Wurster, D. D. Donaldson, M. Collins, D. A. Young, M. J. Grusby, IL-21 limits NK cell responses and promotes antigen-specific T cell activation: A mediator of the transition from innate to adaptive immunity. *Immunity* **16**, 559–569 (2002).
4. R. Zeng, R. Spolski, S. E. Finkelstein, S. Oh, P. E. Kovanen, C. S. Hinrichs, C. A. Pise-Masison, M. F. Radonovich, J. N. Brady, N. P. Restifo, J. A. Berzofsky, W. J. Leonard, Synergy of IL-21 and IL-15 in regulating $CD8^+$ T cell expansion and function. *J. Exp. Med.* **201**, 139–148 (2005).
5. S. Crotty, Follicular helper CD4 T cells (TFH). *Annu. Rev. Immunol.* **29**, 621–663 (2011).
6. K. Ozaki, R. Spolski, R. Ettinger, H.-P. Kim, G. Wang, C.-F. Qi, P. Hwu, D. J. Shaffer, S. Akilesh, D. C. Roopenian, H. C. Morse III, P. E. Lipsky, W. J. Leonard, Regulation of B cell differentiation and plasma cell generation by IL-21, a novel inducer of Blimp-1 and Bcl-6. *J. Immunol.* **173**, 5361–5371 (2004).
7. K. Ozaki, R. Spolski, C. G. Feng, C.-F. Qi, J. Cheng, A. Sher, H. C. Morse III, C. Liu, P. L. Schwartzberg, W. J. Leonard, A critical role for IL-21 in regulating immunoglobulin production. *Science* **298**, 1630–1634 (2002).
8. J. Pesce, M. Kaviratne, T. R. Ramalingam, R. W. Thompson, J. F. Urban Jr., A. W. Cheever, D. A. Young, M. Collins, M. J. Grusby, T. A. Wynn, The IL-21 receptor augments Th2 effector function and alternative macrophage activation. *J. Clin. Invest.* **116**, 2044–2055 (2006).
9. C.-K. Wan, J. Oh, P. Li, E. E. West, E. A. Wong, A. B. Andraski, R. Spolski, Z.-X. Yu, J. He, B. L. Kelsall, W. J. Leonard, The cytokines IL-21 and GM-CSF have opposing regulatory roles in the apoptosis of conventional dendritic cells. *Immunity* **38**, 514–527 (2013).
10. R. Spolski, W. J. Leonard, Interleukin-21: A double-edged sword with therapeutic potential. *Nat. Rev. Drug Discov.* **13**, 379–395 (2014).
11. Y. Chen, F. Yu, Y. Jiang, J. Chen, K. Wu, X. Chen, Y. Lin, H. Zhang, L. Li, Y. Zhang, Adoptive transfer of interleukin-21-stimulated human $CD8^+$ T memory stem cells efficiently inhibits tumor growth. *J. Immunother.* **41**, 274–283 (2018).
12. C. Alvarez-Fernández, L. Escribà-Garcia, S. Vidal, J. Sierra, J. Briones, A short CD3/CD28 costimulation combined with IL-21 enhance the generation of human memory stem T cells for adoptive immunotherapy. *J. Transl. Med.* **14**, 214 (2016).
13. W. Cui, Y. Liu, J. S. Weinstein, J. Craft, S. M. Kaech, An interleukin-21-interleukin-10-STAT3 pathway is critical for functional maturation of memory $CD8^+$ T cells. *Immunity* **35**, 792–805 (2011).
14. Y. Li, C. Yee, IL-21 mediated Foxp3 suppression leads to enhanced generation of antigen-specific $CD8^+$ cytotoxic T lymphocytes. *Blood* **111**, 229–235 (2008).
15. M. H. Hashmi, P. J. Van Veldhuizen, Interleukin-21: Updated review of Phase I and II clinical trials in metastatic renal cell carcinoma, metastatic melanoma and relapsed/refractory indolent non-Hodgkin's lymphoma. *Expert Opin. Biol. Ther.* **10**, 807–817 (2010).
16. G. Isvoranu, M. Chiritoiu-Butnaru, Therapeutic potential of interleukin-21 in cancer. *Front. Immunol.* **15**, 1369743 (2024).
17. T. M. Petrella, R. Tozer, K. Belanger, K. J. Savage, R. Wong, M. Smylie, S. Kamel-Reid, V. Tron, B. E. Chen, N. N. Hunder, L. Hagerman, W. Walsh, E. A. Eisenhauer, Interleukin-21 has activity in patients with metastatic melanoma: A phase II study. *J. Clin. Oncol.* **30**, 3396–3401 (2012).
18. T. M. Petrella, C. L. D. Mihalcioiu, E. McWhirter, K. Belanger, K. J. Savage, X. Song, O. Hamid, T. Cheng, M. L. Davis, C. W. Lee, A. Spatz, J. G. Monzon, L. Hagerman, B. E. Chen, J. Dancey, Final efficacy results of NCIC CTG IND.202: A randomized phase II study of recombinant interleukin-21 (rIL21) in patients with recurrent or metastatic melanoma (MM). *J. Clin. Oncol.* **31**, 9032 (2013).
19. J. M. Coquet, K. Skak, I. D. Davis, M. J. Smyth, D. I. Godfrey, IL-21 modulates activation of NKT cells in patients with stage IV malignant melanoma. *Clin. Transl. Immunology* **2**, e6 (2013).
20. I. D. Davis, B. K. Skrumsager, J. Cebon, T. Nicholaou, J. W. Barlow, N. P. H. Moller, K. Skak, D. Lundsgaard, K. S. Frederiksen, P. Thygesen, G. A. McArthur, An open-label, two-arm, phase i trial of recombinant human interleukin-21 in patients with metastatic melanoma. *Clin. Cancer Res.* **13**, 3630–3636 (2007).
21. J. A. Thompson, B. D. Curti, B. G. Redman, S. Bhatia, J. S. Weber, S. S. Agarwala, E. L. Sievers, S. D. Hughes, T. A. DeVries, D. F. Hausman, Phase I study of recombinant interleukin-21 in patients with metastatic melanoma and renal cell carcinoma. *J. Clin. Oncol.* **26**, 2034–2039 (2008).
22. H. Schmidt, P. Selby, U. Mouritzen, U. H. Thelin, P. E. Kristjansen, P. Geertsen, Subcutaneous (SC) dosing of recombinant human interleukin-21 (rIL-21) is safe and has clinical activity:

Results from a dose-escalation study in stage 4 melanoma (MM) or renal cell cancer (RCC). *J. Clin. Oncol.* **26**, 3041 (2008).
23. S. Bhatia, B. Curti, M. S. Ernstoff, M. Gordon, E. I. Heath, W. H. Miller Jr., I. Puzanov, D. I. Quinn, T. W. Flaig, P. VanVeldhuizen, K. Byrnes-Blake, J. A. Freeman, R. Bittner, N. Hunder, S. Souza, J. A. Thompson, Recombinant interleukin-21 plus sorafenib for metastatic renal cell carcinoma: A phase 1/2 study. *J. Immunother. Cancer* **2**, 2 (2014).
24. W. Hu, J. Wang, J. Dou, X. He, F. Zhao, C. Jiang, F. Yu, K. Hu, L. Chu, X. Li, N. Gu, Augmenting therapy of ovarian cancer efficacy by secreting IL-21 human umbilical cord blood stem cells in nude mice. *Cell Transplant.* **20**, 669–680 (2011).
25. J. M. Timmerman, J. C. Byrd, D. J. Andorsky, M. F. Siadak, T. DeVries, D. F. Hausman, J. M. Pagel, Recombinant interleukin-21 plus rituximab: Clinical activity in a phase 1, dose-finding trial in relapsed low-grade B cell lymphoma. *Blood* **110**, 2577–2577 (2007).
26. C. S. Hinrichs, R. Spolski, C. M. Paulos, L. Gattinoni, K. W. Kerstann, D. C. Palmer, C. A. Klebanoff, S. A. Rosenberg, W. J. Leonard, N. P. Restifo, IL-2 and IL-21 confer opposing differentiation programs to CD8+ T cells for adoptive immunotherapy. *Blood* **111**, 5326–5333 (2008).
27. C. M. Y. Lee, H. McGuire, A. Basten, C. King, D. Christ, Expression, purification and characterization of recombinant interleukin-21. *J. Immunol. Methods* **362**, 185–189 (2010).
28. Z. Chen, Y. Cui, Y. A. Leong, T. Beddoe, D. Yu, Efficient production of recombinant IL-21 proteins for pre-clinical studies by a two-step dilution refolding method. *Int. Immunopharmacol.* **16**, 376–381 (2013).
29. K. Bondensgaard, J. Breinholt, D. Madsen, D. H. Omkvist, L. Kang, A. Worsaae, P. Becker, C. B. Schiødt, S. A. Hjorth, The existence of multiple conformers of interleukin-21 directs engineering of a superpotent analogue. *J. Biol. Chem.* **282**, 23326–23336 (2007).
30. R. Asano, T. Kudo, K. Makabe, K. Tsumoto, I. Kumagai, Antitumor activity of interleukin-21 prepared by novel refolding procedure from inclusion bodies expressed in *Escherichia coli*. *FEBS Lett.* **528**, 70–76 (2002).
31. K. E. Lewis, M. J. Selby, G. Masters, J. Valle, G. Dito, W. R. Curtis, R. Garcia, K. A. Mink, K. S. Waggie, M. S. Holdren, J. F. Grosso, A. J. Korman, M. Jure-Kunkel, S. R. Dillon, Interleukin-21 combined with PD-1 or CTLA-4 blockade enhances antitumor immunity in mouse tumor models. *OncoImmunology* **7**, e1377873 (2017).
32. D.-A. Silva, S. Yu, U. Y. Ulge, J. B. Spangler, K. M. Jude, C. Labão-Almeida, L. R. Ali, A. Quijano-Rubio, M. Ruterbusch, I. Leung, T. Biary, S. J. Crowley, E. Marcos, C. D. Walkey, B. D. Weitzner, F. Pardo-Avila, J. Castellanos, L. Carter, L. Stewart, S. R. Riddell, M. Pepper, G. J. L. Bernardes, M. Dougan, K. C. Garcia, D. Baker, De novo design of potent and selective mimics of IL-2 and IL-15. *Nature* **565**, 186–191 (2019).
33. A. Quijano-Rubio, A. M. Bhuiyan, H. Yang, I. Leung, E. Bello, L. R. Ali, K. Zhangxu, J. Perkins, J.-H. Chun, W. Wang, M. J. Lajoie, R. Ravichandran, Y.-H. Kuo, S. K. Dougan, S. R. Riddell, J. B. Spangler, M. Dougan, D.-A. Silva, D. Baker, A split, conditionally active mimetic of IL-2 reduces the toxicity of systemic cytokine therapy. *Nat. Biotechnol.* **41**, 532–540 (2023).
34. R. Zeng, R. Spolski, E. Casas, W. Zhu, D. E. Levy, W. J. Leonard, The molecular basis of IL-21-mediated proliferation. *Blood* **109**, 4135–4142 (2007).
35. O. J. Hamming, L. Kang, A. Svensson, J. L. Karlsen, H. Rahbek-Nielsen, S. R. Paludan, S. A. Hjorth, K. Bondensgaard, R. Hartmann, Crystal structure of interleukin-21 receptor (IL-21R) bound to IL-21 reveals that sugar chain interacting with WSXWS motif is integral part of IL-21R. *J. Biol. Chem.* **287**, 9454–9460 (2012).
36. D. J. Stauber, E. W. Debler, P. A. Horton, K. A. Smith, I. A. Wilson, Crystal structure of the IL-2 signaling complex: Paradigm for a heterotrimeric cytokine receptor. *Proc. Natl. Acad. Sci. U.S.A.* **103**, 2788–2793 (2006).
37. G. C. Abhiraman, T. U. J. Bruun, N. A. Caveney, L. L. Su, R. A. Saxton, Q. Yin, S. Tang, M. M. Davis, K. M. Jude, K. C. Garcia, A structural blueprint for interleukin-21 signal modulation. *Cell Rep.* **42**, 112657 (2023).
38. S. F. Altschul, W. Gish, W. Miller, E. W. Myers, D. J. Lipman, Basic local alignment search tool. *J. Mol. Biol.* **215**, 403–410 (1990).
39. J. Parrish-Novak, S. R. Dillon, A. Nelson, A. Hammond, C. Sprecher, J. A. Gross, J. Johnston, K. Madden, W. Xu, J. West, S. Schrader, S. Burkhead, M. Heipel, C. Brandt, J. L. Kuijper, J. Kramer, D. Conklin, S. R. Presnell, J. Berry, F. Shiota, S. Bort, K. Hambly, S. Mudri, C. Clegg, M. Moore, F. J. Grant, C. Lofton-Day, T. Gilbert, F. Rayond, A. Ching, L. Yao, D. Smith, P. Webster, T. Whitmore, M. Maurer, K. Kaushansky, R. D. Holly, D. Foster, Interleukin 21 and its receptor are involved in NK cell expansion and regulation of lymphocyte function. *Nature* **408**, 57–63 (2000).
40. H. Asao, C. Okuyama, S. Kumaki, N. Ishii, S. Tsuchiya, D. Foster, K. Sugamura, Cutting edge: The common gamma-chain is an indispensable subunit of the IL-21 receptor complex. *J. Immunol.* **167**, 1–5 (2001).
41. K. A. Casey, M. F. Mescher, IL-21 promotes differentiation of naive CD8 T cells to a unique effector phenotype. *J. Immunol.* **178**, 7640–7648 (2007).
42. H. Elsaesser, K. Sauer, D. G. Brooks, IL-21 is required to control chronic viral infection. *Science* **324**, 1569–1572 (2009).
43. J. Dauparas, I. Anishchenko, N. Bennett, H. Bai, R. J. Ragotte, L. F. Milles, B. I. M. Wicky, A. Courbet, R. J. de Haas, N. Bethel, P. J. Y. Leung, T. F. Huddy, S. Pellock, D. Tischer, F. Chan, B. Koepnick, H. Nguyen, A. Kang, B. Sankaran, A. K. Bera, N. P. King, D. Baker, Robust deep learning-based protein sequence design using ProteinMPNN. *Science* **378**, 49–56 (2022).
44. K. E. Pauken, M. Dougan, N. R. Rose, A. H. Lichtman, A. H. Sharpe, Adverse events following cancer immunotherapy: Obstacles and opportunities. *Trends Immunol.* **40**, 511–523 (2019).
45. S. K. Dougan, M. Dougan, J. Kim, J. A. Turner, S. Ogata, H. I. Cho, R. Jaenisch, E. Celis, H. L. Ploegh, Transnuclear TRP1-specific CD8 T cells with high or low affinity TCRs show equivalent antitumor activity. *Cancer Immunol. Res.* **1**, 99–111 (2013).
46. K. Roehle, L. Qiang, K. S. Ventre, D. Heid, L. R. Ali, P. Lenehan, M. Heckler, S. J. Crowley, C. T. Stump, G. Ro, A. Godicelj, A. M. Bhuiyan, A. Yang, M. Quiles Del Rey, T. Biary, A. M. Luoma, P. T. Bruck, J. F. Tegethoff, S. L. Nopper, J. Li, K. T. Byrne, M. Pelletier, K. W. Wucherpfennig, B. Z. Stanger, J. J. Akin, J. D. Mancias, J. Agudo, M. Dougan, S. K. Dougan, cIAP1/2 antagonism eliminates MHC class I-negative tumors through T cell-dependent reprogramming of mononuclear phagocytes. *Sci. Transl. Med.* **13**, eabf5058 (2021).
47. K. S. Ventre, K. Roehle, E. Bello, A. M. Bhuiyan, T. Biary, S. J. Crowley, P. T. Bruck, M. Heckler, P. J. Lenehan, L. R. Ali, C. T. Stump, V. Lippert, E. Clancy-Thompson, W. D. Conce Alberto, M. T. Hoffman, L. Qiang, M. Pelletier, J. J. Akin, M. Dougan, S. K., Dougan, cIAP1/2 antagonism induces antigen-specific T cell-dependent immunity. *J. Immunol.* **210**, 991–1003 (2023).
48. R. W. Jenkins, A. R. Aref, P. H. Lizotte, E. Ivanova, S. Stinson, C. W. Zhou, M. Bowden, J. Deng, H. Liu, D. Miao, M. X. He, W. Walker, G. Zhang, T. Tian, C. Cheng, Z. Wei, S. Palakurthi, M. Bittinger, H. Vitzthum, J. W. Kim, A. Merlino, M. Quinn, C. Venkataramani, J. A. Kaplan, A. Portell, P. C. Gokhale, B. Phillips, A. Smart, A. Rotem, R. E. Jones, L. Keogh, M. Anguiano, L. Stapleton, Z. Jia, M. Barzily-Rokni, I. Cañadas, T. C. Thai, M. R. Hammond, R. Vlahos, E. S. Wang, H. Zhang, S. Li, G. J. Hanna, W. Huang, M. P. Hoang, A. Piris, J.-P. Eliane, A. O. Stemmer-Rachamimov, L. Cameron, M.-J. Su, P. Shah, B. Izar, M. Thakuria, N. R. LeBoeuf, G. Rabinowits, V. Gunda, S. Parangi, J. M. Cleary, B. C. Miller, S. Kitajima, R. Thummalapalli, B. Miao, T. U. Barbie, V. Sivathanu, J. Wong, W. G. Richards, R. Bueno, C. H. Yoon, J. Miret, M. Herlyn, L. A. Garraway, E. M. Van Allen, G. J. Freeman, P. T. Kirschmeier, J. H. Lorch, P. A. Ott, F. S. Hodi, K. T. Flaherty, R. D. Kamm, G. M. Boland, K.-K. Wong, D. Dornan, C. P. Paweletz, D. A. Barbie, Profiling of PD-1 blockade using organotypic tumor spheroids. *Cancer Discov.* **8**, 196–215 (2018).
49. O.-Y. Revach, A. M. Cicerchia, O. Shorer, C. A. Palin, B. Petrova, S. Anderson, B. Liu, J. Park, L. Chen, A. Mehta, S. J. Wright, N. McNamee, A. Tal-Mason, G. Cattaneo, P. Tiwari, H. Xie, J. M. Sweere, L.-C. Cheng, N. Sigal, E. Enrico, M. Miljkovic, S. A. Evans, N. Nguyen, M. E. Whidden, R. Srinivasan, M. H. Spitzer, Y. Sun, T. Sharova, A. R. Lawless, W. A. Michaud, M. Q. Rasmussen, J. Fang, J. R. Brook, F. Chen, X. Wang, C. R. Ferrone, D. P. Lawrence, R. J. Sullivan, D. Liu, U. M. Sachdeva, D. R. Sen, K. T. Flaherty, R. T. Manguso, L. Bod, M. Kellis, G. M. Boland, K. Yizhak, J. Yang, N. Kanarek, M. Sade-Feldman, N. Hacohen, R. W. Jenkins, Overcoming resistance to immunotherapy by targeting CD38 in human tumor explants. *Cell Rep. Med.* **6**, 102210 (2025).
50. C. T. Kureshi, S. K. Dougan, Cytokines in cancer. *Cancer Cell* **43**, 15–35 (2025).
51. A. M. Bhuiyan, M. Dougan, Engineering T cell memory for antitumor immunity. *Trends Pharmacol. Sci.* **43**, 1–3 (2022).
52. R. Spolski, P. Li, W. J. Leonard, Biology and regulation of IL-2: From molecular mechanisms to human therapy. *Nat. Rev. Immunol.* **18**, 648–659 (2018).
53. R. Kureshi, E. Bello, C. T. S. Kureshi, M. J. Walsh, V. Lippert, M. T. Hoffman, M. Dougan, T. Longmire, M. Wichroski, S. K. Dougan, DGKα/ζ inhibition lowers the TCR affinity threshold and potentiates antitumor immunity. *Sci. Adv.* **9**, eadk1853 (2023).
54. G. K. Antony, A. Z. Dudek, Interleukin 2 in cancer therapy. *Curr. Med. Chem.* **17**, 3297–3302 (2010).
55. J. M. Kirkwood, M. H. Strawderman, M. S. Ernstoff, T. J. Smith, E. C. Borden, R. H. Blum, Interferon Alfa-2b adjuvant therapy of high-risk resected cutaneous melanoma: The eastern cooperative oncology group trial EST 1684. *J. Clin. Oncol.* **41**, 425–435 (2023).
56. B. A. Baldo, Side effects of cytokines approved for therapy. *Drug Saf.* **37**, 921–943 (2014).
57. S. Zhong, K. Malecek, L. A. Johnson, Z. Yu, E. Vega-Saenz de Miera, F. Darvishian, K. McGary, K. Huang, J. Boyer, E. Corse, Y. Shao, S. A. Rosenberg, N. P. Restifo, I. Osman, M. Krogsgaard, T-cell receptor affinity and avidity defines antitumor response and autoimmunity in T-cell immunotherapy. *Proc. Natl. Acad. Sci. U.S.A.* **110**, 6973–6978 (2013).
58. A. E. Moran, K. A. Hogquist, T-cell receptor affinity in thymic development. *Immunology* **135**, 261–267 (2012).
59. J. X. Caushi, J. Zhang, Z. Ji, A. Vaghasia, B. Zhang, E. H.-C. Hsiue, B. J. Mog, W. Hou, S. Justesen, R. Blosser, A. Tam, V. Anagnostou, T. R. Cottrell, H. Guo, H. Y. Chan, D. Singh, S. Thapa, A. G. Dykema, P. Burman, B. Choudhury, L. Aparicio, L. S. Cheung, M. Lanis, Z. Belcaid, M. El Asmar, P. B. Illei, R. Wang, J. Meyers, K. Schuebel, A. Gupta, A. Skaist, S. Wheelan, J. Naidoo, K. A. Marrone, M. Brock, J. Ha, E. L. Bush, B. J. Park, M. Bott, D. R. Jones, J. E. Reuss, V. E. Velculescu, J. E. Chaft, K. W. Kinzler, S. Zhou, B. Vogelstein, J. M. Taube, M. D. Hellmann, J. R. Brahmer, T. Merghoub, P. M. Forde, S. Yegnasubramanian, H. Ji, D. M. Pardoll, K. N. Smith, Transcriptional programs of neoantigen-specific TIL in anti-PD-1-treated lung cancers. *Nature* **596**, 126–132 (2021).
60. B. Dura, S. K. Dougan, M. Barisa, M. M. Hoehl, C. T. Lo, H. L. Ploegh, J. Voldman, Profiling lymphocyte interactions at the single-cell level by microfluidic cell pairing. *Nat. Commun.* **6**, 5940 (2015).
61. M. Dougan, A. M. Luoma, S. K. Dougan, K. W. Wucherpfennig, Understanding and treating the inflammatory adverse events of cancer immunotherapy. *Cell* **184**, 1575–1588 (2021).

62. W. Kabsch, XDS. *Acta Crystallogr. D Biol. Crystallogr.* **66**, 125–132 (2010).
63. I. J. Tickle, A. Sharff, C. Flensburg, O. Smart, P. Keller, C. Vonrhein, W. Paciorek, G. Bricogne, STARANISO (2016); http://staraniso.globalphasing.org/cgi-bin/staraniso.cgi.
64. A. J. McCoy, R. W. Grosse-Kunstleve, P. D. Adams, M. D. Winn, L. C. Storoni, R. J. Read, Phaser crystallographic software. *J. Appl. Cryst.* **40**, 658–674 (2007).
65. M. Yen, J. Ren, Q. Liu, C. R. Glassman, T. P. Sheahan, L. K. Picton, F. R. Moreira, A. Rustagi, K. M. Jude, X. Zhao, C. A. Blish, R. S. Baric, L. L. Su, K. C. Garcia, Facile discovery of surrogate cytokine agonists. *Cell* **185**, 1414–1430.e19 (2022).
66. P. Emsley, B. Lohkamp, W. G. Scott, K. Cowtan, Features and development of Coot. *Acta Crystallogr. D Biol. Crystallogr.* **66**, 486–501 (2010).
67. D. Liebschner, P. V. Afonine, M. L. Baker, G. Bunkóczi, V. B. Chen, T. I. Croll, B. Hintze, L. W. Hung, S. Jain, A. J. McCoy, N. W. Moriarty, R. D. Oeffner, B. K. Poon, M. G. Prisant, R. J. Read, J. S. Richardson, D. C. Richardson, M. D. Sammito, O. V. Sobolev, D. H. Stockwell, T. C. Terwilliger, A. G. Urzhumtsev, L. L. Videau, C. J. Williams, P. D. Adams, Macromolecular structure determination using x-rays, neutrons and electrons: Recent developments in Phenix. *Acta Crystallogr. D Struct. Biol.* **75**, 861–877 (2019).
68. A. Morin, B. Eisenbraun, J. Key, P. C. Sanschagrin, M. A. Timony, M. Ottaviano, P. Sliz, Collaboration gets the most out of software. *eLife* **2**, e01456 (2013).
69. E. Krissinel, K. Henrick, Inference of macromolecular assemblies from crystalline state. *J. Mol. Biol.* **372**, 774–797 (2007).
70. T. D. Goddard, C. C. Huang, E. C. Meng, E. F. Pettersen, G. S. Couch, J. H. Morris, T. E. Ferrin, UCSF ChimeraX: Meeting modern challenges in visualization and analysis. *Protein Sci.* **27**, 14–25 (2018).
71. Y. Sun, O.-Y. Revach, S. Anderson, E. A. Kessler, C. H. Wolfe, A. Jenney, C. E. Mills, E. J. Robitschek, T. G. R. Davis, S. Kim, A. Fu, X. Ma, J. Gwee, P. Tiwari, P. P. Du, P. Sindurakar, J. Tian, A. Mehta, A. M. Schneider, K. Yizhak, M. Sade-Feldman, T. LaSalle, T. Sharova, H. Xie, S. Liu, W. A. Michaud, R. Saad-Beretta, K. B. Yates, A. Iracheta-Vellve, J. K. E. Spetz, X. Qin, K. A. Sarosiek, G. Zhang, J. W. Kim, M. Y. Su, A. M. Cicerchia, M. Q. Rasmussen, S. J. Klempner, D. Juric, S. I. Pai, D. M. Miller, A. Giobbie-Hurder, J. H. Chen, K. Pelka, D. T. Frederick, S. Stinson, E. Ivanova, A. R. Aref, C. P. Paweletz, D. A. Barbie, D. R. Sen, D. E. Fisher, R. B. Corcoran, N. Hacohen, P. K. Sorger, K. T. Flaherty, G. M. Boland, R. T. Manguso, R. W. Jenkins, Targeting TBK1 to overcome resistance to cancer immunotherapy. *Nature* **615**, 158–167 (2023).
72. A. C. M. Domingues, C. Palin, Y. Sun, H. Xie, E. C. Woods, R. W. Jenkins, O.-Y. Revach, Preparation and analysis of monotypic and organotypic tumor spheroids. *Methods Cell Biol.* **196**, 139–159 (2025).
73. M. J. Walsh, C. T. Stump, R. Kureshi, P. Lenehan, L. R. Ali, M. Dougan, D. M. Knipe, S. K. Dougan, IFNγ is a central node of cancer immune equilibrium. *Cell Rep.* **42**, 112219 (2023).
74. J. A. Griffiths, A. C. Richard, K. Bach, A. T. L. Lun, J. C. Marioni, Detection and removal of barcode swapping in single-cell RNA-seq data. *Nat. Commun.* **9**, 2667 (2018).
75. T. Stuart, A. Butler, P. Hoffman, C. Hafemeister, E. Papalexi, W. M. Mauck, Y. Hao, M. Stoeckius, P. Smibert, R. Satija, Comprehensive integration of single-cell data. *Cell* **177**, 1888–1902.e21 (2019).
76. J. W. Squair, M. Gautier, C. Kathe, M. A. Anderson, N. D. James, T. H. Hutson, R. Hudelle, T. Qaiser, K. J. E. Matson, Q. Barraud, A. J. Levine, G. La Manno, M. A. Skinnider, G. Courtine, Confronting false discoveries in single-cell differential expression. *Nat. Commun.* **12**, 5692 (2021).
77. A. T. Lun, K. Bach, J. C. Marioni, Pooling across cells to normalize single-cell RNA sequencing data with many zero counts. *Genome Biol.* **17**, 75 (2016).
78. M. I. Love, W. Huber, S. Anders, Moderated estimation of fold change and dispersion for RNA-seq data with DESeq2. *Genome Biol.* **15**, 550 (2014).
79. A. Liberzon, C. Birger, H. Thorvaldsdóttir, M. Ghandi, J. P. Mesirov, P. Tamayo, The Molecular Signatures Database (MSigDB) hallmark gene set collection. *Cell Syst.* **1**, 417–425 (2015).
80. L. Cao, B. Coventry, I. Goreshnik, B. Huang, W. Sheffler, J. S. Park, K. M. Jude, I. Marković, R. U. Kadam, K. H. G. Verschueren, K. Verstraete, S. T. R. Walsh, N. Bennett, A. Phal, A. Yang, L. Kozodoy, M. DeWitt, L. Picton, L. Miller, E.-M. Strauch, N. D. DeBouver, A. Pires, A. K. Bera, S. Halabiya, B. Hammerson, W. Yang, S. Bernard, L. Stewart, I. A. Wilson, H. Ruohola-Baker, J. Schlessinger, S. Lee, S. N. Savvides, K. C. Garcia, D. Baker, Design of protein-binding proteins from the target structure alone. *Nature* **605**, 551–560 (2022).
81. C. Harly, D. Kenney, G. Ren, B. Lai, T. Raabe, Q. Yang, M. C. Cam, H.-H. Xue, K. Zhao, A. Bhandoola, The transcription factor TCF-1 enforces commitment to the innate lymphoid cell lineage. *Nat. Immunol.* **20**, 1150–1160 (2019).

Acknowledgments

Funding: Supported by funds provided by the National Cancer Institute (R01CA240339) to J.-H.C., A.Q.-R., and D.B.; the National Institute of Allergy and Infectious Disease (R01AI160052) to J.-H.C., S.G., and D.B.; the Division of Intramural Research, National Heart, Lung, and Blood Institute, National Institutes of Health to S.R., P.L., and W.J.L.; the Stanford University Medical Scientist Training Program Grant (T32GM007365) to G.C.A.; Hertz Fellowship to G.C.A.; the National Institutes of Health (R01CA177684) to G.C.A. and M.D.; the National Science Foundation Graduate Research Fellowship to E.C.C.; the Institute for Stem Cell & Regenerative Medicine Graduate Fellowship to E.C.C.; the Washington Research Foundation and Translational Research Fund to A.Q.-R, and D.-A.S.; the Open Philanthropy Project Improving Protein Design Fund to S.G., M.DeW., L.C., and D.B.; the Audacious Project at the Institute for Protein Design to S.G., M.DeW., P.H., L.C., N.P.K., and D.B.; the National Institute of Biomedical Imaging and Bioengineering, the National Institutes of Health, Trailblazer R21 Award (R21EB027327) to H.Y.K.; the National Institutes of Health (R21AI154363, R56AG069194, U01CA281848) to V.K.; the Hopes and Smiles for Kids Foundation to V.K.; the National Institutes of Health (R01AI132819, 5P30CA015704 subaward) to S.S.; the Friedman-Rieger Foundation to S.S.; the National Institutes of Health (R01AI51321) to K.C.G.; the Ludwig Institute for Cancer Research to K.C.G.; Howard Hughes Medical Institute to K.C.G. and D.B.; the National Institutes of Health (R01AI169188-01) to S.K.D. and M.D.; the National Institutes of Health (R01AI158488-01) to S.K.D.; the Melanoma Research Alliance to S.K.D.; the Hale Center for Pancreatic Cancer Research to S.K.D.; the Parker Institute for Cancer Immunotherapy at DFCI to S.K.D. and K.C.G.; the Mark Foundation and the Weill Stanford/UCSF Cancer Innovation Fund to K.C.G; and the Peter and Ann Lambertus Family Foundation to M.D. Additional support provided by the Termeer Early Career Fellowship in Systems Pharmacology to R.W.J., a generous gift from Robert and Marie McInnes to R.W.J., and the MGH ECOR Fund for Medical Discovery Research Fellowship Award to O.-Y.R. Funding is provided by the Massachusetts Life Sciences Center Research Infrastructure Program in support of the Mass General Cancer Center Tumor Cartography Center to R.W.J. This research was supported in part by the Intramural Research Program of the National Institutes of Health. The contributions of the NIH authors were made as part of their official duties as NIH federal employees, are in compliance with agency policy requirements, and are considered works of the United States government. However, the findings and conclusions presented in this paper are those of the authors and do not necessarily reflect the views of the NIH or the US Department of Health and Human Services. **Author contributions:** Conceptualization: J.-H.C., D.-A.S., W.J.L., M.D., S.K.D., and D.B. Methodology: J.-H.C., B.S.L., S.R., M.J.W., G.C.A., T.A., O.-Y.R., E.C.C., P.L., A.K., S.T., G.M.B., T.N., A.Q.-R., K.M.J., L.C., and D.-A.S. Software: J.-H.C., S.R., M.J.W., G.C.A., P.L., K.M.J., and D.-A.S. Validation: J.-H.C., B.S.L., S.R., M.J.W., G.C.A., T.A., O.-Y.R., E.C.C., P.L., A.K., S.T., G.M.B., and K.M.J. Formal analysis: J.-H.C., B.S.L., S.R., M.J.W., G.C.A., K.Z., T.A., E.C.C., P.L., A.K., S.T., R.K., M.T.H., T.N., F.P., J.G.T., S.Y.L., C.J.K., H.S., A.Q.-R., K.M.J., and D.-A.S. Investigation: J.-H.C., B.S.L., S.R., M.J.W., G.C.A., K.Z., T.A., O.-Y.R., E.C.C., P.L., A.K., S.T., R.K., M.T.H., G.M.B., T.N., F.P., J.G.T., S.Y.L., C.J.K., H.S., A.Q.-R., K.M.J., U.Y.U., and D.-A.S. Resources: J.-H.C., S.R., G.C.A., E.C.C., C.A.P., A.K., S.T., T.S., A.L., S.C., G.M.B., S.G., A.M., P.H., and M.D. Writing: J.-H.C., B.S.L., S.R., M.J.W., G.C.A., T.A., E.C.C., N.P.K., H.Y.K., V.K., S.S., R.W.J, G.C.A., K.C.G., W.J.L., M.D., S.K.D., and D.B. wrote the initial manuscript draft. All authors reviewed and revised manuscript drafts. Visualization: J.-H.C., B.S.L., S.R., M.J.W., G.C.A., K.Z., T.A., O.-Y.R., E.C.C., P.L., A.K., S.T., R.K., M.T.H., and K.M.J. Supervision: N.P.K., H.Y.K., V.K., S.S., R.W.J., K.C.G., W.J.L., M.D., S.K.D., and D.B. Project administration: J.-H.C., W.J.L., M.D., S.K.D., and D.B. Funding acquisition: H.Y.K., V.K., S.S., R.W.J., K.C.G., W.J.L., M.D., S.K.D., and D.B. **Competing interests:** J.-H.C., A.Q.-R., U.Y.U., D.-A.S., N.P.K., and D.B. are co-inventors on a US nonprovisional patent application (63/378797) and PCT international application (PCT/US23/76260), which incorporates discoveries described in this manuscript. J.-H.C., A.Q.-R., U.Y.U., D.-A.S., N.P.K., M.D., S.K.D., and D.B. are cofounders and stockholders of Axxis Bio Inc. R.W.J. is a member of the advisory board for and has a financial interest in Xsphera Biosciences Inc., a company focused on using ex vivo profiling technology to deliver functional, precision immune-oncology solutions for patients, providers, and drug development companies. R.W.J. has received honoraria from Incyte (invited speaker), G1 Therapeutics (advisory board), Bioxcel Therapeutics (invited speaker). R.W.J. has ownership interest in US Patents US20200399573A9 and US20210363595A1. R.W.J.'s interests were reviewed and are managed by Massachusetts General Hospital and Mass General Brigham in accordance with their competing interest policies. A.Q.-R. and D.-A.S. have employment with Monod Bio Inc. unrelated to this project. M.J.W. reports employment with Nuvalent unrelated to this project. S.K.D. received research funding unrelated to this project from Novartis, BMS, and Takeda and was a founder, science advisory board member, and equity holder in Kojin. M.D. has research funding from Eli Lilly; he has received consulting fees from Genentech, ORIC Pharmaceuticals, Partner Therapeutics, SQZ Biotech, AzurRx, Eli Lilly, Mallinckrodt Pharmaceuticals, Aditum, Foghorn Therapeutics, Palleon, and Moderna; and he is a member of the Scientific Advisory Board for Neoleukin Therapeutics, Veravas, and Cerberus Therapeutics. The remaining authors declare that they have no competing interests. **Data and materials availability:** All data and information needed to support the paper are present in the manuscript or the Supplementary Materials. The crystal structure has been deposited in the RCSB protein data bank with accession code PDB ID: 9E2T. RNA-seq has been deposited in the Gene Expression Omnibus (GEO) under the accession number GSE256289. scRNA-seq has been deposited in the GEO under the accession number GSE240834, with its code deposited in both Zenodo (DOI: 10.5281/zenodo.15690716; https://zenodo.org/records/15690716) and GitHub (https://github.com/mjlwalsh/21h10_scRNAseq). Tabulated data underlying the figures are provided in data file S1. Uncropped immunoblots are provided in data file S2. All other data needed to support the conclusions of the paper are present in the paper or the Supplementary Materials. IL-21 variants are available upon request from the corresponding authors.

Submitted 3 March 2025
Accepted 4 September 2025
Published 26 September 2025
10.1126/sciimmunol.adx1582